Computers and Geotechnics 66 (2015) 96–112

Contents lists available at ScienceDirect

Computers and Geotechnics

journal homepage: www.elsevier.com/locate/compgeo

A robust finite volume model to simulate granular flows

S. Yavari-Ramshe [a,*], B. Ataie-Ashtiani [a], B.F. Sanders [b]

[a] Department of Civil Engineering, Sharif University of Technology, PO Box 11155-9313, Tehran, Iran
[b] The Henry Samueli School of Engineering, Department of Civil and Environmental Engineering, University of California, Irvine, USA

ARTICLE INFO

Article history:
Received 21 June 2014
Received in revised form 10 November 2014
Accepted 22 January 2015
Available online 11 February 2015

Keywords:
Finite volume method
Mudslide
Granular flow
Landslide
Coulomb friction law

ABSTRACT

This paper introduces a well-balanced second-order finite volume scheme, based on the *Q*-scheme of Roe, for simulating granular type flows. The proposed method is applied to solve the incompressible Euler equations under Savage–Hutter assumptions. The model is derived in a local coordinate system along a non-erodible bed to take its curvature into account. Moreover, simultaneous appearance of flowing/static regions is simulated by considering a basal friction resistance which keeps the granular flow from moving when the angle of granular flow is less than the angle of repose. The proposed scheme preserves stationary solutions up to second order and deals with different situations of wet/dry transitions by a modified nonlinear wet/dry treatment. Numerical results indicate the improved properties and robustness of the proposed finite volume structure. In addition, the granular flow properties are estimated with a computational error of less than 5%. These errors are consistently less than those obtained by using similar existing finite volume schemes without the proposed modifications, which can result in up to 30% overestimation.

1. Introduction

Natural granular flows like landslides, mudslides, snow avalanches and rockslides are natural hazards that may impose fatalities and significant economical damages. These flows are associated with soil erosion and sedimentation into rivers and valleys [1,18,33], seabed topography change, and soil or surface/ground water contamination [64]. Moreover, on the shores of a water body, they may be followed by resulting impulsive waves and their subsequent dam overtopping [6,7,9–11,14,63,82] or run-up to coastal areas [36,80] as a secondary hazard. In order to conduct hazard analysis and protect settled areas, predictions of the flow thickness and velocity of the slide are needed [58,62,72]. To this end, a number of numerical studies have been performed based on different numerical approaches.

Savage and Hutter [70] pioneered the study of rock, snow and ice avalanches based on shallow water equations under hydrostatic assumption, using two finite difference methods, one of Lagrangian and the other of Eulerian. Their theory was verified to be in an excellent agreement with laboratory experiments [39,46,52,70]. Many of the available numerical models apply the Savage–Hutter (SH) type considerations to describe the behavior of granular type flows [30,44,45,58,65,75,81]. This fact also confirms the ability and efficiency of these assumptions in recitation of the granular flow behavior [51]. SH type models are based on the shallow water equations considering a Coulomb friction term as the flow/bottom interaction [70]. The constitutive relation of the granular material is also defined based on the Mohr–Coulomb criteria; i.e. the normal stresses are related to the longitudinal stresses by a factor K (the earth pressure coefficient) [70]. In 1991, the SH formulation was transferred to a local coordinate system for considering the bed curvature effects [71]. Gray et al. [38] extended this model to two dimensions. Wieland et al. [81] used a mixed FVM–FDM (Finite Volume Method–Finite Difference Method) to discretize the two dimensional SH model. The effects of the bed erosion were inserted in this model by Pitman et al. [65] who applied a Godunov type FVM to discretize the model equations. Denlinger and Iverson [31] extended the three dimensional version of a SH type model using Harten, Lax and Van Leer contact (HLLC) finite volume scheme. More studies have been performed on behavior of granular type flows based on different rheologies and governing equations using FDM [2,42,49,62,75], FVM [23,32,53,58,61,83], FEM (Finite Element Method) [4,27,28,35], SPH (Smoothed Particle Hydrodynamics) [59], or a combination of these schemes [3,81].

A comprehensive review of these studies is summarized in Table 1. This table shows the previous numerical models including their governing equations, considered rheology, numerical

* Corresponding author. Tel.: +1 (714) 861 9220; fax: +98 (21) 6601 4828.
E-mail addresses: yavari@mehr.sharif.edu (S. Yavari-Ramshe), ataie@sharif.edu (B. Ataie-Ashtiani), bsanders@uci.edu (B.F. Sanders).

http://dx.doi.org/10.1016/j.compgeo.2015.01.015
0266-352X/

Nomenclature

A	coefficient matrix
b	bottom level
c	characteristic wave velocity
D	diagonal matrix of eigenvalues
df	generalized Roe flux difference
Err	computational error
F	numerical flux matrix
G	source term matrix
G_1	source term matrix concerning bed level
G_2	source term matrix concerning bed curvature
G_3	first θ related part of the flux term
G_4	second θ related part of the flux term
$\vec{g}$	gravitational acceleration vector
g	gravitational acceleration
H	granular flow depth vertical to the bed
H'	characteristic depth
h	granular flow depth $(h')/\cos^2\theta$
h'	granular flow depth
I	computational cell
Id	identity matrix
J	Jacobean of transformation matrix
K	earth pressure coefficient
κ	eigenvector
L	characteristic length
m	number of computational grids
n	number of time steps
n_s	unit normal vector of flow surface
n_b	unit normal vector of bottom
P	pressure tensor
P_{XX}	normal pressure along X
P_{ZZ}	normal pressure along Z
P_{ZX}	longitudinal stress along X
P_{XZ}	longitudinal stress along Z
P_{xx}	normal pressure along x
P_{zz}	normal pressure along z
P_{zx}	longitudinal stress along x
P_{xz}	longitudinal stress along z
P_1	$\kappa D \kappa^{-1}$
$P^{\pm}$	projection matrixes $1/2\kappa(Id \pm \mathrm{sgn}(D))\kappa^{-1}$
Q	matrix characteristic of a Q scheme
q	flow discharge hu
$\bar{q}$	depth-averaged flow discharge $h\bar{u}$
q^*	predicted flow discharge in the first step
r	$\Delta t/\Delta x$
S	numerical source term matrix
S_1	numerical source term matrix related to bed level
S_2	numerical source term matrix related to bed curvature
S_3	1st numerical θ related part of the flux term matrix
S_4	2nd numerical θ related part of the flux term matrix
T	Coulomb friction matrix
T^*	Coulomb friction matrix of the corrector step
t	time
U	flow velocity parallel to the bottom
U_b	sliding velocity along bottom
$\bar{U}$	depth-averaged velocity parallel to bottom
u	horizontal flow velocity
$\bar{u}$	Roe-averaged velocity
V	flow velocity perpendicular to the bottom
V'	flow velocity vector (u, v)
v	vertical flow velocity
W	unknown matrix $[hq]$
W^*	predicted values in the first step $[hq^*]$
W^+	exact solution of nonlinear Riemann problem in the right edge of wet/dry transition intercell
W^-	exact solution of nonlinear Riemann problem in the left edge of wet/dry transition intercell
X	local coordinate component along non-erodible bed
$\vec{X}$	cartesian coordinate vector (x,z)
$\vec{X}'$	local coordinate vector (X,Z)
x	horizontal component of Cartesian coordinate system
Y_1	a state value
Y_2	a state value
Z	local coordinate component perpendicular to the bed
z	vertical component of Cartesian coordinate system
ρ	density of granular mass
θ	local slope angle of the bed
δ	basal friction angle
δ_0	angle of repose
ϕ	internal friction angle of granular material
ϕ'	a numerical flux function
ε	small parameter of dimensional analysis
$\Im$	Coulomb friction term
σ_c	critical friction resistance of bottom
λ	eigenvalue
Δx	computational cell size
Δt	computational time step
τ_{crit}	critical longitudinal stress of the bottom
∇	gradient vector $(\partial/\partial x, \partial/\partial z)$
γ	a small parameter $\in (0, 1)$

approaches and numerical schemes. Based on this review, FVM and FEM have been more popular than FDM because of using the integral form of conservation laws which is closer to the physics [55,73]. FVM has also the advantage of preserving conservation of mass and momentum in multidimensional physical systems like granular avalanches where rapid transitions between flowing and static states are common [55]. The new approach of SPH, which has been lately used by many researchers, e.g. [5,8,12,13,59], is not efficient in simulating the situations where flow encounters unexpected corners or constrictions [30].

The SH type formulations are applied in the present model to describe the behavior of the granular flow. The present SH type model has two special properties. It takes bed curvature effects and flow dynamic/static regions into account. Based on the previous studies, bottom curvatures have noticeable effects on the behavior of granular type flows [20,30,34,42,67]. Lately, two new SH models have been introduced by Bouchut et al. [20] over a general bottom. The first model considers small variations of the bed curvature and the second one is dealing with general bottom topographies. The present SH type model applied the first hypothesis, i.e. a small variation of the curvature. Accordingly, the model equations are derived in a local coordinate system along with the bed to take its curvature into account. This model differs from original SH model through a new curvature term which is required to obtain the energy inequality and to satisfy the stationary solutions regarding water at rest [20]. Moreover, in the present model, a critical stress is defined to stop the granular layer from moving when its angle is less than the angle of repose [19,34]. This second property is especially important when the flow is supposed to be shallow which results in simultaneous existence of the flowing and the static regions [72].

Effective and robust numerical solution of the system of model equations described above is the main focus of this paper. A well-balanced finite volume scheme is proposed which minimize the

Table 1
A review of the numerical studies on granular flows.

Ref. no.	Developer name	Year	Rheology	Governing equations	Numerical method	Numerical scheme	Model dim.	Application	Case study
70	Savage & Hutter	1989	Coulomb friction	SWE	FDM	L	1D	Rock, snow and ice avalanches	–
45	Hutter & Greve	1993	Coulomb friction	SWE	FDM	–	2D	Rock, snow and ice avalanches	–
42	Hungr	1995	Vary along the slide path	SWE	FDM	L	1D	Granular flow	1
53	Laigle & Coussot	1997	Herschel-Bulkley	SWE	FVM	Godunov	1D	Mudflow	–
81	Wieland et al.	1999	Coulomb friction	SWE	M FV-FD	L	2D	Granular avalanche	–
38	Gray et al.	1999	Coulomb friction	SWE	FDM	L	2D	Granular avalanche	–
23	Brufau et al.	2000	Manning's Eq.	SWE	FVM	Roe	1D	Debris flows	–
49	Imran et al.	2001	Herschel-Bulkley/bilinear	PSFA	FDM	L	1D	Muddy debris flows	–
30	Denlinger & Iverson	2001	Coulomb friction	SWE	FVM	HLLC	3D	Debris flows/rock avalanches	–
35	Frenette et al.	2002	Drucker-Parger type	NSE	FEM	Galerkin	1D	Granular flow	–
2	Aranson et al.	2002	Bagnold	SWE	FDM	–	1D/2D	Partially fluidized granular flows	–
83	Zanuttigh & Lamberti	2003	Bingham/Herschel–Bulkley/ Visco-plastic	SWE	FVM	WAF	1D	Debris flow	–
65	Pitman et al.	2003	Coulomb friction	SWE	FVM	Godunov	2D	Granular avalanche/ landslides	1
58	Mangeney et al.	2003	Coulomb friction	SWE	FVM	K	1D	Granular avalanche	–
28	Chen & Lee	2003	Voellmy	SWE	LFEM	–	3D	Landslide	1
59	McDougall & Hungr	2004	Bingham/Voellmy/frictional/ plastic	SWE	SPH	–	3D	Landslide	–
31	Denlinger & Iverson	2004	Coulomb friction	SWE	FVM	HLLC	3D	Granular avalanche	–
75	Toni & Scotton	2005	Coulomb friction	SWE	FDM	L	2D	Snow avalanche	1
61	Medina et al.	2008	Bingham/Herschel–Bulkley/ Voellmy	SWE	FVM	Godunov	2D	Debris flows	3
62	Moriguchi et al.	2009	Bingham	NSE	FDM	THINC	2D	Debris flow	–
3	Armanini et al.	2009	Grain-inertial	SWE	H FV-FE	–	2D	Debris flow	2
32	Domnik et al.	2013	Coulomb-Viscoplastic	NSE	FVM	MC	2D	Granular flow	–
27	Chauchat & Medale	2014	$\mu(1)$	SWE	FEM	–	3D	Dense granular flow	–
4	Armanini et al.	2014	Modified Coulomb type	SWE	FEM	Galerkin	–	Satu. granular flow	–

FVM: Finite Volume Method, NSE: Navier–Stokes Equations, HLL: Harten, Lax and Van Leer, FDM: Finite Difference Method, SWE: Shallow Water Equations, LHLL: Lateralized HLL, FEM: Finite Element Method, PSFA: Prandtl's Slender Flow Approximations, HLLC: HLL Contact, LFEM: Lagrangian FEM, M FV-FD: Mixed FV-FD method, MC: Marker and Cell method, H FV-FE: Hybrid FV-FE method, WAF: Weighted Average Flux method, L: Lagrangian, SPH: Smoothed Particle Hydrodynamics, THINC: Tangent of Hyperbola for Interface Capturing, K: Kinetic.

appearance of negative flow depth, spurious waves and artificial dispersion, especially in the situations involving shocks, discontinuities, high gradients or wet/dry fronts [55,76]. In simulating the granular type flows, we are dealing with a hyperbolic system of conservation laws with source terms to solve a series of the Riemann problems and determine the local wave structure [55]. The most frequent approximate Riemann solvers are Roe scheme [68] and Harten, Lax and Van Leer (HLL) scheme [40]. A difficulty of HLL type models is modeling the full Riemann solution by only two waves based on approximate speeds of the fastest and slowest waves in each cell [76]. Therefore, in the present study, the proposed numerical framework is been developed based on a Roe type scheme as a better choice, especially for the systems with more than two equations like Euler equations or multi dimensional flows [55,76].

One of the main challenges related to the discretization of a hyperbolic system of conservation laws with source terms is dealing with the heterogeneous part; i.e. the source terms. In the present model due to considering an arbitrary topography, there are three different source terms involving the bottom geometry, the bed curvature and the basal friction. Centered discretization of the source terms yields to appearance of spurious numerical waves [16,69,79]. Upwinding the source terms in a similar way to the numerical flux can overcome this deficiency [16]. This idea was introduced by Roe [69] in 1986 and was applied into Saint–Venant equations by Glaister [37]. With upwinding the source terms the numerical scheme will have a bigger stable region [69]. Bermudez and Vazquez-Cendon [16] applied this idea for shallow water equations using the Q-scheme of Roe and Van Leer. Vázquez-Cendón [79] extended this model with considering three source terms including the bottom level, the breadth function and the bed friction, in a rectangular open channel. He showed that centered discretization of each source term can be a source of appearance of artificial waves [79]. The second complexity related to the numerical treatment of the source terms is discretization of the Coulomb friction term; particularly, with considering no movement for granular material in the cells where its angle is less than the angle of repose. It can originate numerical instabilities during the simulation [34]. This problem is solved by applying a two-step semi-implicit method proposed by Mangeney-Castelnau et al. [58] and applied by Fernández-Nieto et al. [34].

The second numerical intricacy is appearance of wet/dry fronts during the simulation of the shallow granular type flows. Wet/dry fronts appear along numerical domain where the avalanche depth vanishes, due to initial condition or as a consequence of the landslide motion (Fig. 3a) [25]. These fronts may originate negative values of flow thickness which yields to numerical instabilities [56]. Besides, the numerical scheme may not be able to preserve steady or near steady flows including wet/dry fronts [24,25]. Bermudez and Vazquez-Cendon [16] introduced a concept called conservation property (C-property). A numerical scheme satisfies this condition if it correctly solves the steady state solutions related to water at rest [16]. Hence, a well balanced numerical scheme should satisfy the C-property condition. In the present

study, the proposed method of Castro et al. [25] is applied as a new treatment of wet/dry fronts. In this method, at every intercell with wet/dry transition a nonlinear Riemann problem is considered which is easy to solve. The exact solutions of these nonlinear Riemann problems are employed to calculate the numerical fluxes. Although a big variety of wetting and drying algorithms have been proposed before, most of them are not general [15,22,24,77], or linearly extrapolate the flow depth onto dry cells [17,60]. The applied method of Castro et al. [25] has two distinctive advantages: using nonlinear Riemann problem instead of a usual linear one at intercells where a wet/dry transition happens and modifying the numerical scheme at all related situations not only when the bottom emerges at intercell [25]. We have modified this wet/dry algorithm for dealing with the bed curvature source term in the present model.

Finally, for the sake of simplicity, the problems are simulated in one dimension. However, the proposed scheme can be extended for more general one dimensional or multi dimensional flows. The only drawback is complication of using the considered wet/dry method for multi dimensional flows. In these situations, the wet/dry fronts can be treated by an approximation of the present wet/dry algorithm proposed by [24].

The core objective of this work is to introduce a robust and effective Roe type finite volume method for granular flow modeling so that improves the shortcomings of previous similar formulations. The key novelty of this work is implementing an effective combination of the state of the art of numerical methods such as: numerical treatment of non-homogeneous source terms, wet/dry fronts, and friction term considering flowing/static regions. The resulting method is a well-balanced scheme that minimizes the appearance of negative flow depths and spurious numerical waves or dispersion which are likely to appear during the simulation of landslides where flow moves on a dry bed and may encounter with many natural or man-made obstacles or adverse slopes. The paper is organized as follows: Section 2 provides the governing mathematical equations. In Section 3, we present a well-balanced finite volume scheme based on the Q-scheme of Roe, to discretize the system of model equations. Section 4 is devoted to performing a series of numerical and experimental tests to illustrate the improved properties of the proposed numerical scheme in preserving the stationary solutions, treating wet/dry fronts and estimating the granular flow properties. It is also shown that how upwinding the source term related to the bed curvature helps the numerical stability of the proposed scheme. Finally, the concluding results will be discussed in the last section.

2. Mathematical model equations

The following incompressible Euler equations are considered to derive the system of model equations [76].

$$\begin{cases} \nabla \cdot V' = 0 \\ \rho \partial_t V' + \rho V' \cdot \nabla V' = -\nabla \cdot P + \rho \nabla (\vec{g} \cdot \vec{X}) \end{cases} \tag{1}$$

where $V' = (u, v)$ is the velocity vector with the horizontal and the vertical components u and v. ρ is the constant density of the granular material, $P = \begin{bmatrix} P_{xx} & P_{xz} \\ P_{zx} & P_{zz} \end{bmatrix}$ is the pressure tensor with $P_{xz} = P_{zx}$ and $\vec{g} = (0, -g)$ is the vector of gravitational acceleration. $\vec{X} = (x, z)$ represents Cartesian coordinate. $\nabla = (\frac{\partial}{\partial x}, \frac{\partial}{\partial z})$ is the gradient vector. t is time and $\partial_t = \frac{\partial}{\partial t}$. The model parameters are illustrated in Fig. 1.

Eq. (1) is transferred to a local coordinate system over the non-erodible bed defined by $z = b(x)$, based on the following transformation matrix [34]

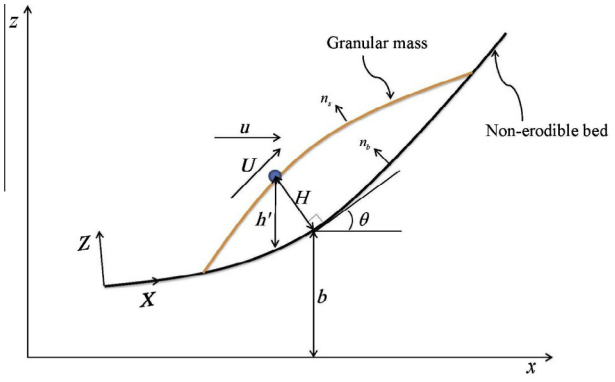

Fig. 1. Schematic definition of the present model parameters.

$$\nabla_{\vec{X}}(X, Z) = \frac{1}{J} \begin{pmatrix} \cos\theta & \sin\theta \\ -J\sin\theta & J\cos\theta \end{pmatrix}, \quad J = 1 - Z d_X \theta \tag{2}$$

X and Z are the components of this local coordinate system. X denotes the arc's length of the bottom and Z is measured perpendicular to the bed (Fig. 1). J is the Jacobian of the change of variables. It should be noticed that for a non-erodible bed, the depth of the sliding mass cannot exceed the local radius of the bed curvature for $J \neq 0$ [71]. The incompressible Euler equations in the new coordinate system are [34]

$$\begin{cases} \partial_X U + \partial_Z (JV) = 0 \\ \rho \partial_t (JU) + \rho \partial_X (U^2) + \rho \partial_Z (JVU) + \rho \partial_X (\vec{g} \cdot \vec{X}') \\ = -\partial_X (P_{XX}) - \partial_Z (JP_{ZX}) \\ \quad + \rho V (\partial_X (U\theta) + \partial_Z (JV\theta)) + P_{XZ} d_X \theta \\ \rho \partial_t (JV) + \rho \partial_X (UV) + \rho \partial_Z (JV^2) + \rho J \partial_Z (\vec{g} \cdot X') \\ = -\partial_X (P_{XZ}) - \partial_Z (JP_{ZZ}) \\ \quad - \rho U (\partial_X (U\theta) + \partial_Z (JV\theta)) - P_{XX} d_X \theta \end{cases} \tag{3}$$

where U and V are the flow velocity components parallel and perpendicular to the bottom, respectively. θ is the local bed slope. $\partial_Z = \partial/\partial Z$, $\partial_X = \partial/\partial X$ and $\vec{X}' = (X, Z)$ represents the local coordinate system.

The following kinematic (K.C.) and boundary (B.C.) conditions are considered at the granular flow surface [70]

$$\begin{cases} \partial_t H + U \partial_X H - V = 0 & \text{K.C.} \\ P \cdot n_S = 0 & \text{B.C.} \end{cases} \tag{4}$$

and at the bottom [70]

$$\begin{cases} V = 0 & \text{K.C.} \\ P \cdot n_b - n_b (n_b \cdot P \cdot n_b) = -(U_b/|U_b|)(n_b \cdot P \cdot n_b) \tan\delta & \text{B.C.} \end{cases} \tag{5}$$

where n_S and n_b are the exterior unit normal vector of the flow surface and the bottom, respectively. H is the granular flow thickness vertical to the bed. The second equation of Eq. (5) describes the interactions between the granular flow and the non-erodible bottom based on a Coulomb type friction law [70]. In this relation, U_b is the sliding velocity along the stationary bed and δ is the basal friction angle.

In the next step, the system of model Eq. (3) and the boundary conditions (4) and (5) are given in dimensionless form, using two characteristic lengths of L and H' in the X and Z direction, respectively. The non-dimensional variables $\sim$ are as follows [34]:

$$(X, Z, t) = (L\widetilde{X}, H'\widetilde{Z}, \sqrt{L/g}\widetilde{t}), \quad (U, V) = \sqrt{Lg}(\widetilde{U}, \varepsilon\widetilde{V}),$$

$$(P_{XX}, P_{ZZ}) = gH'(\widetilde{P}_{XX}, \widetilde{P}_{ZZ}), \quad P_{XZ} = gH' \tan\delta_0 \widetilde{P}_{XZ}, \quad H = H'\widetilde{H}$$

δ_0 is the angle of repose of the granular material [34]. $\varepsilon = H'/L$ is supposed to be a small value due to considering a shallow domain. Based on this change of variables, the non-dimensional system of model Eq. (3) will be [34]

$$\begin{cases} \partial_{\tilde{X}}\tilde{U} + \partial_{\tilde{Z}}(J\tilde{V}) = 0 \\ \tilde{J}\partial_t(\rho\tilde{U}) + \rho\tilde{U}\partial_{\tilde{X}}(\tilde{U}) + \rho\tilde{J}\tilde{V}\partial_{\tilde{Z}}(\tilde{U}) + \rho\partial_{\tilde{X}}(b + \tilde{Z}\cos\theta + \tilde{P}_{\tilde{X}\tilde{X}}/\rho)\varepsilon \\ \quad = -\tan\delta_0\partial_{\tilde{Z}}(\tilde{J}\tilde{P}_{\tilde{X}\tilde{Z}}) + \rho\tilde{V}\varepsilon\tilde{U}d_{\tilde{X}}\theta + \varepsilon\tan\delta_0\tilde{P}_{\tilde{X}\tilde{Z}}\partial_{\tilde{X}}\theta \\ \varepsilon[\tilde{J}\partial_t(\rho\tilde{V}) + \rho\tilde{U}\partial_{\tilde{X}}(\tilde{V}) + \rho\tilde{V}\partial_{\tilde{Z}}(\tilde{V}) + \partial_{\tilde{X}}(\tilde{P}_{\tilde{X}\tilde{X}}) - \tilde{P}_{\tilde{X}\tilde{X}}\partial_{\tilde{X}}\theta - P_{\tilde{Z}\tilde{Z}}d_{\tilde{X}}\theta] \\ \quad +\rho\tilde{J}\partial_{\tilde{Z}}(b + \cos\theta\tilde{Z}) = -J\partial_{\tilde{Z}}(\tilde{P}_{\tilde{Z}\tilde{Z}}) - \rho\tilde{U}^2d_{\tilde{X}}\theta \end{cases} \tag{6}$$

The dimensionless form of the exterior unit vector of the granular flow surface is $n_s = (-\varepsilon\partial_{\tilde{X}}\tilde{H}, 1)/\sqrt{1+\varepsilon^2(\partial_{\tilde{X}}\tilde{H})^2}$. Therefore, the non-dimensional boundary and kinematic conditions at the flow surface from Eq. (4) are [34]

$$\begin{cases} \partial_t\tilde{H} + \tilde{U}\partial_{\tilde{X}}\tilde{H} - \tilde{V} = 0 & \text{K.C.} \\ -\varepsilon\partial_{\tilde{X}}\tilde{H}\tilde{P}_{\tilde{X}\tilde{X}} + \tan\delta_0\tilde{P}_{\tilde{Z}\tilde{X}} = 0 & \text{B.C.} \\ -\varepsilon\tan\delta_0\partial_{\tilde{X}}\tilde{H}\tilde{P}_{\tilde{X}\tilde{Z}} + \tilde{P}_{\tilde{Z}\tilde{Z}} = 0 & \text{B.C.} \end{cases} \tag{7}$$

and at the bottom from Eq. (5) [34]

$$\begin{cases} \tilde{V} = 0 & \text{K.C.} \\ \tan\delta_0\tilde{P}_{\tilde{X}\tilde{Z}} = -(\tilde{U}_b/|\tilde{U}_b|)\tilde{P}_{\tilde{Z}\tilde{Z}}\tan\delta_0 & \text{B.C.} \end{cases} \tag{8}$$

In the following equations tilde ($\sim$) is omitted for simplicity. In the present model, the constitutive behavior of the granular material is defined as $P_{XX} = KP_{ZZ}$, where K represents the earth pressure coefficient as [70]

$$K = 2\left(1 - \mathrm{sgn}(\partial U/\partial X)\sqrt{1-(\cos\phi/\cos\delta)^2}\right)/\cos^2\phi - 1 \tag{9}$$

ϕ represents the internal friction angle of the granular material. In this equation, the "active" and "passive" states of the earth pressure coefficient are correspond to the maximum and minimum values of K which are distinguished by the sign of the longitudinal strain ($\mathrm{sgn}(\partial U/\partial X)$) [70]. There are additional improved techniques for distinction between the two states like the gradual transition introduced by Hungr [42,59] which improves the numerical model stabilities. In the present study, we have applied a two step scheme to satisfy numerical stability of the proposed scheme regarding the Coulomb friction term.

Now, the third relation of Eq. (6) is integrated along the flow depth. As it mentioned in Section 1, $d_X\theta$ is considered to be $O(\varepsilon)$ [20,34]. Therefore,

$$P_{ZZ} = \rho(H - Z)\cos\theta \tag{10}$$

With substituting Eqs. (9) and (10) into the first two relations of Eq. (6), we have

$$\begin{aligned} &\partial_t(\rho U) + \rho\partial_X U^2 + \rho\partial_Z(UV) + \rho\partial_X(b + Z\cos\theta + K(H-Z)\cos\theta)\varepsilon \\ &= -\tan\delta\partial_Z(P_{XZ}) \end{aligned} \tag{11}$$

In the next step, the equations are depth-averaged in perpendicular direction to the bottom. The averaged values of velocity are defined as $\breve{U} = \frac{1}{H}\int_0^H U(X,Z)dZ$ and $\breve{U^2} = \frac{1}{H}\int_0^H U^2(X,Z)dZ$ [70].

Now, the constitutive relations, boundary and kinematic conditions are substituted into the system of model Eq. (6) to obtain the depth-averaged system of model equations. $d_X\theta$ is considered to be $O(\varepsilon)$ [20]; therefore, $J = 1 - Zd_X\theta \approx 1$ [34]. The coulomb friction term is also assumed to be order of some $\gamma \in (0,1)$; this is $\tan\delta_0 = O(\varepsilon^\gamma)$. Based on these considerations, the depth-averaged form of the system of model equations is

$$\begin{cases} \partial_t H + \partial_X(H\breve{U}) = 0 \\ \partial_t(H\breve{U}) + \partial_X(H\breve{U^2} + \varepsilon K(H^2/2)\cos\theta) \\ = -\varepsilon H d_X b + \varepsilon(H^2/2)\sin\theta d_X\theta \\ \quad -(H\cos\theta + H\breve{U}2d_X\theta)(U_b/|U_b|)\tan\delta + O(\varepsilon^{1+\gamma}) \end{cases} \tag{12}$$

Now, the system of model Eq. (12) is rewritten with original variables as the system of model Eq. (13). In this form, the terms of order $\varepsilon^{1+\gamma}$ are neglected and the profile of the flow velocity is considered to be constant [34].

$$\begin{cases} \partial_t H + \partial_X(H\breve{U}) = 0 \\ \partial_t(H\breve{U}) + \partial_X\left(H\breve{U^2} + gK\frac{H^2}{2}\cos\theta\right) = -gHd_X b + g\frac{H^2}{2}\sin\theta d_X\theta \\ -(gH\cos\theta + H\breve{U^2}d_X\theta)(U_b/|U_b|)\tan\delta \end{cases} \tag{13}$$

As the final step, the system of model Eq. (13) is returned to the global Cartesian coordinate system using the following relations [34].

$$\partial/\partial X = \cos\theta\partial/\partial x, \quad h = H/\cos\theta, \quad \breve{q} = h\breve{u}$$

Consequently, the final system of model equations will be

$$\begin{cases} \partial_t h + \partial_x(\breve{q}\cos\theta) = 0 \\ \partial_t\breve{q} + \partial_x(h\breve{u^2}\cos\theta + gKh^2/2\cos^3\theta) \\ = -gh\cos\theta d_x b + gh^2/2\sin\theta\cos^2\theta\partial_x\theta + \Im/\cos\theta \end{cases} \tag{14}$$

where $\Im$ represents the Coulomb friction term which is defined as follows [34]

$$\begin{cases} \Im = -(gh\cos^2\theta + h\cos\theta\breve{u^2}d_x(\sin\theta))\frac{\breve{q}}{|\breve{q}|}\tan\delta & |\Im| \geqslant \sigma_c \\ q = 0 & |\Im| < \sigma_c \end{cases} \tag{15}$$

where σ_c is the basal critical stress which is defined based on the angle of repose of the sliding mass as $\sigma_c = gh\cos^2\theta\tan\delta_0$ [34]. Eq. (15) shows that when the basal friction term is less than the critical basal stress, $|\Im| < \sigma_c$, the granular mass stops moving, $u = 0$. This condition happens when the granular mass angle is smaller than the angle of repose [34].

3. Numerical model formulations

In this section, we propose a modified Q-scheme of Roe to discretize the system of model Eq. (14). Eq. (14) can be re-written in the form of a hyperbolic system with a conservative product, F and three source terms, G_1, G_2 and T corresponding to the bed level, the bed curvature and the basal friction, respectively. It should be noticed that the tilde ($\breve{}$) has been omitted in the following equations.

$$\partial_t W + \partial_x F(\theta, W) = G_1(x, W) + G_2(x, W) + T \tag{16}$$

where

$$W = \begin{bmatrix} h \\ q \end{bmatrix}, \quad F(\theta, W) = \begin{bmatrix} q\cos\theta \\ \frac{q^2}{h}\cos\theta + gK\frac{h^2}{2}\cos^3\theta \end{bmatrix}$$

$$G_1 = \begin{bmatrix} 0 \\ -gh\cos\theta d_x b \end{bmatrix}, \quad G_2 = \begin{bmatrix} 0 \\ -g\frac{h^2}{4}\cos\theta\partial_x(\cos^2\theta) \end{bmatrix} \text{ and}$$

$$T = \begin{bmatrix} 0 \\ \Im/\cos\theta \end{bmatrix}$$

As it mentioned in the introduction section, the source terms G_1 and G_2 are upwinded in the same way of the flux term, F. For numerical discretization of the Coulomb friction term T, a two-step semi-implicit approach is applied [34,58]. In the first step, the unknowns are calculated without considering the basal friction effects. Then, in the second step, the predicted flow velocity is modified based on Eq. (15) [34]. In this stage, if the granular material angle is less than the angle of repose, the flow velocity becomes zero.

Definition of the flux term, F, shows that it is not only a function of the vector of unknowns, but also a function of the bed slope, $\theta(x)$. The system of model Eq. (14) can be expanded as

$$\begin{cases} \partial_t h + \partial_x(q)\cos\theta = -q\partial_x(\cos\theta) \\ \partial_t q + \partial_x(hu^2)\cos\theta + \partial_x(gKh^2/2)\cos^3\theta \\ = -hu^2\partial_x(\cos\theta) - 3gKh^2/4\cos\theta\partial_x(\cos^2\theta) \\ \quad -gh\cos\theta d_x b - gh^2/4\cos\theta\partial_x(\cos^2\theta) + \Im/\cos\theta \end{cases} \tag{17}$$

The non-conservative form of the model Eq. (17) is

$$\partial_t W + A(\theta, W)\partial_x W = G(\theta, W) \tag{18}$$

where $G(\theta, W) = G_1 + G_2 + \partial_\theta F + T$ and $\partial_\theta F = G_3 + G_4$.

$$G_3 = \begin{bmatrix} 0 \\ -3gk\frac{h^2}{4}\cos\theta\partial_x(\cos^2\theta) \end{bmatrix}, \quad G_4 = \begin{bmatrix} -q\partial_x(\cos\theta) \\ -\frac{q^2}{h}\partial_x(\cos\theta) \end{bmatrix}$$

$A(\theta, W)$ is the Jacobean matrix of the system of model Eq. (14) as

$$A(\theta,W) = \begin{bmatrix} 0 & \cos\theta \\ -u^2\cos^2\theta + gkh^2\cos^3\theta & 2u\cos\theta \end{bmatrix} = \begin{bmatrix} 0 & 1 \\ -u^2+c^2 & 2u \end{bmatrix}\cos\theta \tag{19}$$

In this matrix $u = q/h$ is the averaged velocity of the flow. The local eigenvalues, λ_l, and the local eigenvectors, κ_l, of the coefficient matrix A can be calculated as

$$\lambda_l = [u \pm c]\cos\theta \text{ and } \kappa_l = \begin{bmatrix} 1 \\ u \pm c \end{bmatrix} \tag{20}$$

where $c = (gKh\cos^2\theta)$ is a specific wave speed and $l = 1, 2$.

The computational domain is subdivided into constant intervals of size Δx as shown in Fig. 2. The ith grid cell is denoted by $I_i = [x_{i-1/2}, x_{i+1/2}]$ [55]. For the sake of simplicity, the time step, Δt, is also supposed to be constant and $t_n = n\Delta t$. $x_{i+1/2} = i\Delta x$ and $x_i = (i - 1/2)\Delta x$ is the center of the cell I_i. W_i^n denotes the numerical approximation of the average value over the ith cell at time t^n as [55]

$$W_i^n \cong \frac{1}{\Delta x}\int_{x_{i-1/2}}^{x_{i+1/2}} W(x, t^n)dx \tag{21}$$

3.1. Modified Q-scheme of Roe

The Q-schemes are a family of three point upwind schemes corresponding to numerical fluxes, ϕ', of the form [16]

$$\phi'(Y_1, Y_2) = \frac{F(Y_1) - F(Y_2)}{2} - \frac{1}{2}|Q(Y_1, Y_2)|(Y_1 - Y_2) \tag{22}$$

For each Q-scheme, Q is a matrix characteristic having a continuous dependence on the two state values of Y_1 and Y_2. For example, in the Roe scheme which is based on a linearization of the flux, Q is a diagonalizable matrix which satisfies the property of conservation across discontinuities as follows [76],

$$F(Y_1) - F(Y_2) = Q(Y_1, Y_2)(Y_1 - Y_2) \tag{23}$$

Roe proposed to define Q as the Jacobian matrix, A, evaluated at some state $\widehat{W} = \widehat{W}(Y_1, Y_2)$ known as the Roe average of Y_1 and Y_2 [76].

3.1.1. First step

The primitive form of the proposed modified Q-scheme of Roe with upwinding the source terms for the system of model Eq. (14) is [31,38]

$$\begin{aligned} W_i^* = W_i^n + r\left(F_{i-1/2}^{n+1/2} - F_{i+1/2}^{n+1/2}\right) + r\left(P_{i-1/2}^{+}S_{i-1/2}^{n} + P_{i+1/2}^{-}S_{i+1/2}^{n}\right) \\ + r\left(P_{2,i-1/2}^{+}T_{i-1/2}^{n}dx + P_{2,i+1/2}^{-}T_{i+1/2}^{n}dx\right) \end{aligned} \tag{24}$$

$W_i = [h_i \quad q_i]$ is the unknown matrix, $W_i^* = \left[h_i^{n+1} \quad q_i^*\right]$ is the predicted states at the first step and $r = dt/dx$. The numerical fluxes are calculated as [16]

$$F_{i\pm1/2} = \frac{1}{2}\{F(W_{i\pm1}) - F(W_i) - P_{1,i+1/2}dW_{i+1/2}\} \tag{25}$$

where $P_{1,i+1/2} = \kappa_{i+1/2}|D_{i+1/2}|\kappa_{i+1/2}^{-1}, dW_{i+1/2} = W_{i+1} - W_i$ and $|D_{i+1/2}| = \begin{bmatrix} |\lambda_{1,i+1/2}| & 0 \\ 0 & |\lambda_{2,i+1/2}| \end{bmatrix}$. In this diagonal matrix $\lambda_{i+1/2}$, and $\kappa_{i+1/2}$, are the local eigenvalues and eigenvectors of the Jacobean matrix $A_{i+1/2}$ which is

$$A_{i+1/2} == \begin{bmatrix} 0 & 1 \\ -\bar{u}_{i+1/2}^2 + c_{i+1/2}^2 & 2\bar{u}_{i+1/2} \end{bmatrix}\cos\theta_{i+1/2} \tag{26}$$

The coefficient matrix A is evaluated at the Roe's intermediate states:

$$\bar{u}_{i+1/2} = \frac{\sqrt{h_{i+1}}u_{i+1} + \sqrt{h_i}u_i}{\sqrt{h_{i+1}} + \sqrt{h_i}}, \quad h_{i+1/2} = \frac{h_{i+1} + h_i}{2},$$

$$\cos\theta_{i+1/2} = \frac{\cos\theta_i + \cos\theta_{i+1}}{2}, \cos^2\theta_{i+1/2} = \frac{\cos^2\theta_i + \cos^2\theta_{i+1}}{2},$$

$$c_{i+1/2}^n = \sqrt{gK\frac{h_{i+1}^n + h_i^n}{2}\cos^2\theta_{i+1/2}}$$

The numerical source term is given by

$$\begin{aligned} S_{i+1/2} &= S_{1,i+1/2} + S_{2,i+1/2} + \partial_\theta F_{i+1/2} \\ &= S_{1,i+1/2} + S_{2,i+1/2} + S_{3,i+1/2} + S_{4,i+1/2} \end{aligned} \tag{27}$$

where

$$S_{1,i+1/2} = \begin{bmatrix} 0 \\ -gh_{i+1/2}\cos\theta_{i+1/2} \end{bmatrix}db_{i+1/2},$$

$$S_{2,i+1/2} = \begin{bmatrix} 0 \\ -gh_{i+1/2}^2/4\cos\theta_{i+1/2} \end{bmatrix}d(\cos^2\theta)_{i+1/2},$$

$$S_{3,i+1/2} = \begin{bmatrix} 0 \\ -3gKh_{i+1/2}^2/4\cos\theta_{i+1/2} \end{bmatrix}d(\cos^2\theta)_{i+1/2},$$

$$S_{4,i+1/2} = \begin{bmatrix} -q_{i+1/2} \\ -q_{i+1/2}^2/h_{i+1/2} \end{bmatrix}d(\cos\theta)_{i+1/2}$$

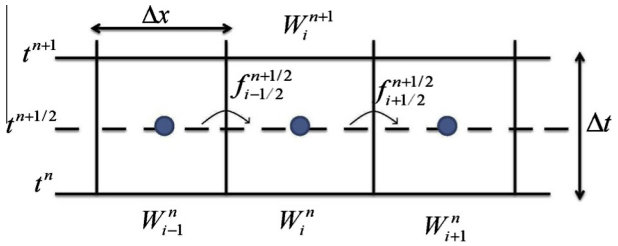

Fig. 2. Illustration of the proposed finite volume method for updating the cell average W_i^n by the intermediate values of fluxes $f_{i\pm1/2}^{n+1/2}$ at the cell edges, shown in x–t space.

and

$$db_{i+1/2} = b_{i+1} - b_i, \quad d(\cos\theta)_{i+1/2} = \cos\theta_{i+1} - \cos\theta_i, d(\cos^2\theta)_{i+1/2} = \cos^2\theta_{i+1} - \cos^2\theta_i$$

The numerical source term, $G_{i+1/2}$, is upwinded by applying the projection matrices [38]

$$P^{\pm}_{i+1/2} = \frac{1}{2}\kappa_{i+1/2}(Id \pm \mathrm{sgn}(D_{i+1/2}))\kappa^{-1}_{i+1/2} \tag{28}$$

where Id is the identity matrix and $\mathrm{sgn}(D_{i+1/2}) = \begin{bmatrix} \mathrm{sgn}(\lambda_{1,i+1/2}) & 0 \\ 0 & \mathrm{sgn}(\lambda_{2,i+1/2}) \end{bmatrix}$.

$T_{i+1/2}$ is the Coulomb friction term defined as $T_{i+1/2} = \begin{bmatrix} o \\ \Im_{i+1/2}/\cos\theta_{i+1/2} \end{bmatrix}$, where [34]

$$\Im_{i+1/2} = \begin{cases} \Im_{1,i+1/2} + \Im_{2,i+1/2} & \text{if } |q_{i+1/2}| > \frac{\Delta t \sigma_{c,i+1/2}}{\cos\theta_{i+1/2}} \\ \tau_{crit,i+1/2} & \text{otherwise} \end{cases} \tag{29}$$

and [34]

$$\Im_{1,i+1/2} = -gh_{i+1/2}\cos^2\theta_{i+1/2}\mathrm{sgn}(\bar{u}_{i+1/2})\tan\delta$$

$$\Im_{2,i+1/2} = -h_{i+1/2}\bar{u}^2_{i+1/2}\frac{\sin\theta_{i+1} - \sin\theta_i}{\Delta x}\mathrm{sgn}(\bar{u}_{i+1/2})\tan\delta\cos\theta_{i+1/2}$$

$$\sigma_{c,i+1/2} = gh_{i+1/2}\cos^2\theta_{i+1/2}\tan\delta_0$$

$$\begin{aligned}\tau_{crit,i+1/2} = gh_{i+1/2}\cos^2\theta_{i+1/2}\{&K(b_{i+1} - b_i + h_{i+1}\cos^2\theta_{i+1} \\ &- h_i\cos^2\theta_i)/\Delta x + (1-K)((b_{i+1} - b_i)/\Delta x \\ &+ (h_{i+1/2}/4)(\cos^2\theta_{i+1} - \cos^2\theta_i)/\Delta x\}\end{aligned}$$

In the first step, the Coulomb friction term is only included in the Roe correction part [34] with the projection matrix:

$$P^{\pm}_{2,i+1/2} = \pm\frac{1}{2}\kappa_{i+1/2}\mathrm{sgn}(D_{i+1/2})\kappa^{-1}_{i+1/2} \tag{30}$$

The proposed Q-scheme of Roe can be re-written in a more general form as

$$W^*_i = W^n_i + r\left(df^{n+1/2,+}_{i-1/2} - df^{n+1/2,-}_{i+1/2}\right) \tag{31}$$

where $W^{n+1/2}_i$ is supposed to be the vector of unknowns computed at the first step for $\frac{dt}{2}\left(W^{n+1/2}_i = W^n_i + \frac{r}{2}\left(df^{n,+}_{i-1/2} - df^{n,-}_{i+1/2}\right)\right)$ and $df^{n+1/2,\mp}_{i\pm1/2} = df^{\mp}_{i\pm1/2}\left(W^{n+1/2}_i, W^{n+1/2}_{i\pm1}\right)$ is a generalized Roe flux difference computed as

$$\begin{aligned}\mathrm{df}^{n+1/2,\mp}_{i+1/2} = \frac{1}{2}\{&\pm F^{n+1/2}_{i+1} \mp F^{n+1/2}_i \pm S^n_{i+1/2} - P_{1,i+1/2}\mathrm{dW}^{n+1/2}_{i+1/2} \\ &+ P_{2,i+1/2}(S^n_{i+1/2} + T^n_{i+1/2}\mathrm{dx})\}\end{aligned} \tag{32}$$

The vector of unknowns, $W^*_i = \begin{bmatrix} h^*_i & q^*_i \end{bmatrix}$, is calculated by Eq. (32) without considering the interaction between the granular material and the non-erodible bed which is defined by the Coulomb friction term, T. In the second step, the granular flow heights remain the same, i.e. $h^{n+1}_i = h^*_i$, but the predicted values of flow velocity, q^*_i, will be modified based on the effects of the Coulomb friction to compute the state values corresponding to the next time step, $W^{n+1}_i = \begin{bmatrix} h^{n+1}_i & q^{n+1}_i \end{bmatrix}$.

3.1.2. Second step

In this step, the state values, $W^*_i = \begin{bmatrix} h^*_i & q^*_i \end{bmatrix}$, predicted in the first step, are applied to calculate the updated values of flow velocity q^{n+1}_i, based on the following equations [34].

$$q^{n+1}_i = \begin{cases} (q^*_i + \left(\Im^*_{1,i} + \Im^*_{2,i}\right)\Delta t/\cos\theta_i & \text{if } |q^*_i| > \sigma^*_{c,i}\Delta t/\cos\theta_i \\ 0 & \text{otherwise} \end{cases} \tag{33}$$

where [34]

$$\Im^*_{1,i} = -0.5\{(c^*_{i-1/2})^2 + (c^*_{i+1/2})^2\}\cos\theta_i\mathrm{sgn}(q^*_i)\tan\delta$$

$$\begin{aligned}\Im^*_{2,i} = &-0.5(h^*_{i-1/2} + h^*_{i+1/2})u^{*2}_i(\sin\theta_{i+1/2} - \sin\theta_{i-1/2})\mathrm{sgn}(q^*_i) \\ &\times \tan\delta\cos\theta_i/\Delta x\end{aligned}$$

$$\begin{aligned}\sigma^*_{c,i} &= 0.5\{(c^*_{i-1/2})^2 + (c^*_{i+1/2})^2\}\cos\theta_i\tan\delta_0, \quad c^*_{i+1/2} \\ &= \sqrt{g(h^*_i + h^*_{i+1})/2\cos\theta_{i+1/2}}\end{aligned}$$

Now the state values of the next time step, $W^{n+1}_i = \begin{bmatrix} h^{n+1}_i & q^{n+1}_i \end{bmatrix}$, are calculated. Observe that when the Coulomb friction term is less than the critical resistance of the bottom against the flow, $|T| < \sigma_c$, the granular material stops moving, $q = 0$. In fact, the numerical treatment of the Coulomb friction term acts like a predictor–corrector method. In the first step, this term is only considered in the uncentered part of the scheme. Then, the predicted value of q^*_i is corrected using Eq. (33) in the second step.

3.2. Numerical scheme properties

More considerations and properties of the proposed numerical scheme are as follows:

3.2.1. Order of accuracy

The scheme introduces a second-order approximation of the system of model Eq. (14) in both space and time, $W^{n+1}_i = W^n_i + \mathrm{O}(\Delta x^2, \Delta t^2)$. To achieve the second order of accuracy in time, the intermediate values of fluxes at $t^{n+1/2}$, $F^{n+1/2}_{i+1/2}$ and $F^{n+1/2}_{i-1/2}$, are applied for updating the state values, W^n_i, based on the numerical approach introduced by Lax and Wendroff in 1960 [54].

3.2.2. CFL condition

Regarding the stability requirements, the following CFL (Courant–Friedrichs–Lewy) condition is applied in the present model [29]

$$\max\{\|\lambda_{l,i\pm1/2}\|_\infty, 1 \leqslant l \leqslant 2, 0 \leqslant i \leqslant m\}\Delta t/\Delta x \leqslant \gamma \tag{34}$$

where $0 < \gamma \leqslant 1$ is a constant, $\lambda_{l,i\pm1/2}$ is the eigenvalues of the Jacobean matrix A and m is the number of computational cells.

3.2.3. Critical flow fix

In Roe-type schemes, the fluxes may not be computed correctly when the flow is critical [21] or more generally when one of the eigenvalues of the Jacobean matrix A goes to zero [26]. As it is well known, the Froude number of a critical flow, $Fr = u/c$, is equal to one [55]. It means that one of the eigenvalues, $\lambda_1 = (u - c)\cos\theta$, of the Jacobean matrix A vanishes in the intercells where the flow is critical. When any of the eigenvalues of the Jacobean matrix A are zero, the numerical viscosity of the scheme disappears which may cause inappropriate numerical behavior in these situations [26]. The most applied correction for these situations is the Harten regularization [41]. He proposed to increase the near zero eigenvalues based on the following equation by choosing a small parameter ε' [41].

$$|\lambda|^* = |\lambda| + 0.5\left\{(1 + \mathrm{sgn}(\varepsilon' - |\lambda|)\left(\frac{\lambda^2 + \varepsilon'^2}{2\varepsilon'} - |\lambda|\right)\right\} \tag{35}$$

In this method ε' should be selected arbitrary. In the present model, a better numerical solution is applied which increases the near zero eigenvalues in critical cells based on the right, λ^R, and the left, λ^L, eigenvalues of the critical cell [78] as

$$|\lambda|^* = \frac{\lambda^2}{\Delta\lambda} + \frac{\Delta\lambda}{4} \quad \text{When} \quad -\Delta\lambda/2 < \lambda < \Delta\lambda/2 \tag{36}$$

where $\Delta\lambda = 4(\lambda^R - \lambda^L)$ [78]. Then, the flux terms are computed based on these modified eigenvalues $|\lambda|^*$.

3.2.4. Wet/dry treatment

As it mentioned before, the proposed method of Castro et al. [25] is employed for numerical treatment of wet/dry fronts, in the present model. In this approach, a simple nonlinear Riemann problem will be considered at intercells where wet/dry transitions happen. The exact solutions of this problem are applied to calculate the numerical fluxes at the related intercell [25].

In Roe type schemes, with Roe linearization of the Jacobean matrix a linear Riemann problem is considered in each intercell, $x_{i+1/2}$, as follows [76]

$$\begin{cases} \partial_t W + A\partial_x W = 0 \\ W(x,t^n) = W_i^n & x < x_{i+1/2} \\ W(x,t^n) = W_{i+1}^n & x > x_{i+1/2} \end{cases} \tag{37}$$

When a wet/dry front is detected in the intercell $x_{i+1/2}$, i.e. $h_i > 0$ and $h_{i+1} = 0$, the linear Riemann problem (37) is replaced by a nonlinear one [25]:

$$\begin{cases} \partial_t W + \partial_x F(W) = 0 \\ W(x,t^n) = W_i^n & x < x_{i+1/2} \\ W(x,t^n) = W_{i+1}^n & x > x_{i+1/2} \end{cases} \tag{38}$$

The choice of these nonlinear problems relies on the bed level, $b(x)$, at the both sides of the wet/dry front [25]. As it can be observed in Fig. 3, W^+ and W^- are considered to be the exact solutions at the right and the left sides of the intercell $x_{i+1/2}$ where a wet/dry transition is happening. A summary of the exact solutions corresponding to these nonlinear problems at different situations are as follows [25].

(a) The bottom is flat; i.e. $b_i = b_{i+1}$ [25]

$$W^+ = W^- = \begin{cases} \begin{bmatrix} 0 \\ 0 \end{bmatrix} & u_i < -2c_i \\ \begin{bmatrix} (u_i + 2c_i)^2/9g \\ (u_i + 2c_i)^3/27g \end{bmatrix} & -2c_i \leqslant u_i < c_i \\ W_i & u_i \geqslant c_i \end{cases} \tag{39}$$

where $c_i = \sqrt{gKh_i \cos^2\theta_i}$ is the characteristic wave speed.

(b) The flow is moving down a slope; i.e. $b_i > b_{i+1}$ [25]

$$W^+ = W^- = \begin{bmatrix} 0 \\ 0 \end{bmatrix} \text{ if } u_i < -2c_i \tag{40}$$

$$W^- = \begin{bmatrix} h_0 \\ q_0 \end{bmatrix} = \begin{bmatrix} (u_i + 2c_i)^2/9g \\ (u_i + 2c_i)^3/27g \end{bmatrix} \text{ and } W^+ = \begin{bmatrix} h' \\ q_i \end{bmatrix} \text{ if } -2c_i \leqslant u_i < c_i \tag{41}$$

where h' is the greatest root of the polynomial (42). In this case, the flow is critical at the left edge of the intercell and subcritical at the right edge [25].

$$P_L(h') = h'^3 + (b_{i+1} - b_i - Q_0^2/(2gh_0^2) - h_0)h'^2 + q_0^2/(2g) \tag{42}$$

$$W^- = W_i \text{ and } W^+ = \begin{bmatrix} h' \\ q_i \end{bmatrix} \text{ if } u_i \geqslant c_i \tag{43}$$

where h' is the least positive root of the following polynomial. In this case, the flow is supercritical in both sides of the intercell [25].

$$P_L(h') = h'^3 + \left(b_{i+1} - b_i - q_i^2/(2gh_i^2) - h_i\right)h'^2 + q_i^2/(2g) \tag{44}$$

(c) The granular flow is moving up a slope; i.e. $b_i < b_{i+1}$ [25]

$$W^- = \begin{bmatrix} \tilde{h} \\ 0 \end{bmatrix}$$

$$\text{where } \tilde{h} = \begin{cases} o & u_i \leqslant -2c_i \\ (u_i/2 + c_i)/g & -2c_i < u_i \leqslant 0 \\ h' & u_i > 0 \end{cases} \text{ and } W^+ = \begin{bmatrix} 0 \\ 0 \end{bmatrix} \tag{45}$$

where h' is the greatest root of the following polynomial [25]:

$$P_L(h') = h'^3 - h_i h'^2 - h_i^2 h' + h_i^3 - 2q_i^2 h'/(gh_i) \tag{46}$$

In this case, the granular flow is not able to move forward, because either the slope acts as an obstacle for the flow if [25]

$$\begin{cases} u_i \leqslant 0 \\ b_{i+1} \geqslant h_i + b_i \end{cases} \tag{47}$$

or the wet cell has no enough mechanical energy if [25]

$$\begin{cases} u_i \geqslant 0 \\ b_{i+1} - b_i > h_i + q_i^2/(2gh_i^2) - 3q_i^{2/3}/(2g^{1/3}) \end{cases} \tag{48}$$

$$W^- = W_i \text{ and } W^+ = \begin{bmatrix} h' \\ q_i \end{bmatrix} \tag{49}$$

where h' is the least positive root of the following polynomial [25]:

$$P_L(h') = h'^3 + \left(b_i - b_{i+1} - q_i^2/(2gh_i^2) - h_i\right)h'^2 + q_i^2/(2g) \tag{50}$$

In this case, the flow is supercritical in the wet cell. It has enough mechanical energy to advance toward the slope and go up. This situation happens when [25]

$$\begin{cases} u_i > 0 \\ b_{i+1} - b_i < h_i + q_i^2/(2gh_i^2) - 3q_i^{2/3}/(2g^{1/3}) \end{cases} \tag{51}$$

In the last case, the granular flow has energy enough to go up the slope. The nonlinear Riemann problem in this condition is not easy to solve. Therefore, the scheme is applied without any modifications [25].

It should be noted that in all the mentioned cases corresponding to wet/dry transitions, the bed level at the left and the right edges of the intercell, where a wet/dry transition happens, are supposed to be the same as the bed level at the left and the right mesh points, respectively (Fig. 3) [25]. In fact, it is supposed that there is a step in the related intercell. In Fig. 3, a wet/dry front is considered in intercell $x_{i+1/2}$, i.e. ith cell is a wet cell ($h_i \neq 0$) and ($i+1$)th cell is a dry one ($h_{i+1} \neq 0$). Since $b_i < b_{i+1}$, the case (c) of the wet/dry treatment should be considered. Hence, the exact solutions of the nonlinear Riemann problems, $W^{\pm}$, can be calculated by Eqs. (45)–(51).

In the present model, there is another source term related to the bed curvature, S_2, which also affects the wet/dry transitions. We propose to presume no curvature at the both sides of the related intercell for calculating the numerical fluxes, $df_{i+1/2}^{\mp}$. As it is shown in Fig. 3, a flat bed can be presumed in the both sides of the intercell containing a wet/dry transition. The present numerical results demonstrate that with this modification, the proposed numerical scheme becomes a complete well-balanced scheme. It satisfies all

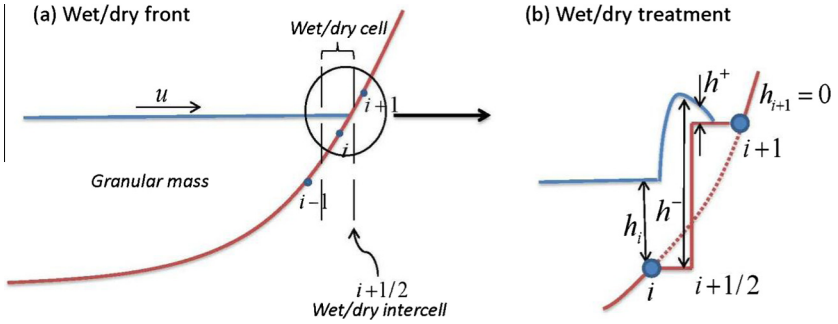

Fig. 3. (a) An example of a wet/dry front and (b) the local change of the bed topography because of the considered numerical wet/dry treatment; $W_i = [h_i\, q_i] \neq 0$ and $W_{i+1} = [h_{i+1}\, q_{i+1}] = 0$ are the state values at the ith and $i+1$th mesh points, respectively. $W^- = [h^-\, q^-]$ and $W^+ = [h^+\, q^+]$ are the exact solutions of the considered non-linear Riemann problem at the left and the right sides of wet/dry intercell $x_{i+1/2}$, which are applied to calculate the numerical fluxes in the wet/dry cell i.

the stationary solutions regarding water at rest with or without wet/dry transitions. It is also able to deal with all different cases of wet/dry transitions.

3.2.5. Stationary solutions

Considering no movement for the granular mass means $u(x) = 0$. In this condition, the system of model Eq. (17) results in

$$\partial_x\left(gK\frac{h^2}{2}\right)\cos^3\theta = -\frac{3}{4}gKh^2\cos\theta\partial_x(\cos^2\theta) - gh\cos\theta d_x b - g\frac{h^2}{4}\cos\theta\partial_x(\cos^2\theta) + \frac{\Im}{\cos\theta} \tag{52}$$

where $\Im < \sigma_c = gh\cos^2\theta\tan\delta_0$. Which leads to the following inequality.

$$|K\cos^2\theta\partial_x h + \frac{3K+1}{4}h\partial_x(\cos^2\theta) + d_x b| \leqslant \tan\delta_0 \tag{53}$$

which is a first order differential equation and can be easily solved for each arbitrary boundary condition. This relation demonstrates dependence of stationary flow surface profile on the values of K and the bed curvature. It confirms that the flow surface slope should be smaller than $\tan\delta_0$ [34]. When $K = 1$, the surface profile is independent of the bed curvature:

$$|\partial_x(b + h\cos^2\theta)| \leqslant \tan\delta_0 \tag{54}$$

When the fluid is water, i.e. $\delta = \phi = 0$, the stationary solution verifies,

$$\begin{cases} u(x) = 0 \\ b(x) + h'(x) = cst \end{cases} \tag{55}$$

where $h'(x) = H(x)\cos\theta(x) = h(x)\cos^2\theta(x)$. For a granular material, since the inequality (53) is satisfied, there will be no movement in the granular material and the flow surface will be preserved. Otherwise, the granular profile will transfer to a new stable state depending on the values of the bed curvature, the internal and the basal friction angles so that its angle becomes less than the angle of repose all over the non-erodible bottom.

For better understanding of the performance of the present model using the proposed scheme, its flowchart has been illustrated in Fig. 4. As it can be seen in this flowchart, the distinctive modifications made to the general Q-scheme of Roe [38] in the present model are:

- Using the intermediate flux terms, $df^{n+1/2,\mp}_{i\pm1/2} = df^{\mp}_{i\pm1/2}(W^{n+1/2}_i, W^{n+1/2}_{i\pm1})$, to update the state values up to second order in both time and space.
- Upwinding the source term S_2 related to the bed curvature in the same way of flux terms.
- Applying the nonlinear wet/dry algorithm of Castro et al. [25] modified for dealing with the bed curvature.
- Altering the critical flow simulation by the proposed method of Van Leer et al. [78].
- Employing a two-step semi-implicit discretization for the source term T including the Coulomb friction effects and considering the simultaneous flowing/static regions of the granular flow by a critical basal resistance term, based on the proposed method of Fernández-Nieto et al. [34].

4. Numerical tests

In this section, a series of experimental results and numerical tests are simulated using the present model to verify the improved properties of the proposed scheme. The ability of the model in preserving the stationary solutions, dealing with different situations of wet/dry transitions, critical flows and adverse slopes is been examined in the following numerical simulations. The estimated values of granular flow thicknesses, velocities, maximum run up and final deposition profile is also compared with their experimental measurements. It should be mentioned that in all the following simulated cases, the runtime is less than 2 min with a 2.2 GHz Intel Core 2 CPU.

4.1. Stationary solutions

To confirm the ability of the proposed scheme in preserving the steady state corresponding to water at rest, i.e. $u = 0$ and $b + h\cos^2\theta = cst$, a simple numerical test is performed as follows. An arc-shaped slope (1 m radius) is considered in order to have variable values of both the bed slope and the bed curvature. Consequently, all the source terms are involved in simulation. The bottom topography and the initial conditions are defined as (Fig. 5a)

$$b(x) = \sqrt{1-(x-1)^2} - 1, \quad h(x) = \begin{cases} 0 & b(x) \geqslant 0.235 \\ 0.235 - b(x) & b(x) < 0.235 \end{cases}, \quad u(x) = 0 \tag{56}$$

The model parameters are chosen as $\Delta x = 0.01$ and $r = dt/dx = 0.1$. At first, we suppose no internal and basal friction angles ($\phi = \delta = 0$). It means that we have a layer of water at rest. It helps to make sure that the scheme is a complete well-balanced scheme. The numerical results are illustrated in Fig. 5. As it can be observed in Fig. 5b, considering no wet/dry treatment leads to numerical instability due to appearance of negative heights at the place of wet/dry transition. On the other hand, with applying the proposed wet/dry treatment of Castro et al. [25], no negative height emerges to make the numerical results unstable. Nevertheless, the steady state solution is not still satisfied completely. As it mentioned in Section 3.2, in the present model, there is a new source term regarding the bed curvature

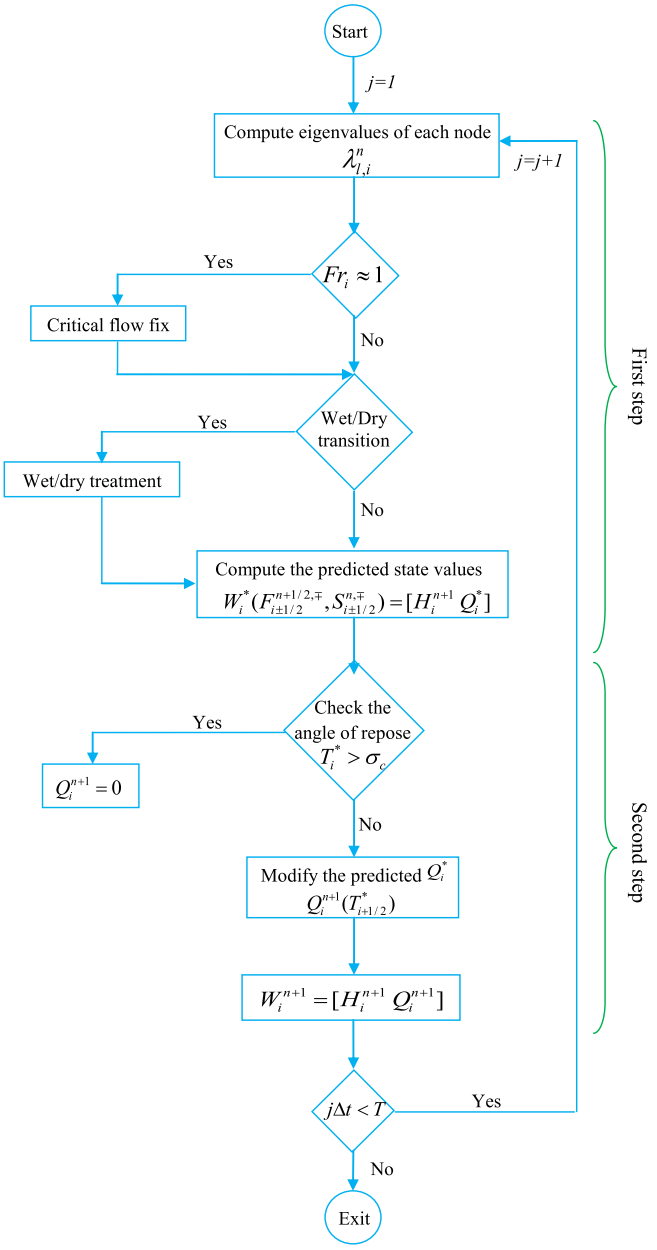

Fig. 4. The proposed scheme flowchart, T is the considered computational time.

which should be also treated properly when a wet/dry transition happens. The artificial numerical wave caused by this term in the wet/dry front is exemplified in Fig. 5c. In accordance with Fig. 3, when a wet/dry transition occurs, for example at intercell $x_{i+1/2}$, it is proposed to consider no bed curvature for calculating the numerical fluxes $df^{\pm}_{i+1/2}$ at the left and the right sides of the intercell, in the present model. With this modification the proposed numerical scheme becomes totally well-balanced.

For a granular mass with the same initial condition, since the inequality (53) is satisfied there will be no movement in the granular material and the scheme preserves the flow surface profile as it is shown in Fig. 5a. The constant value of 30° is been considered as the basal friction angle, δ. With the same conditions as Eq. (56) and the same model parameters, the new stable states of granular mass with different values of K are shown in Fig. 6. For $K < 1.5$ in combination with the considered bottom curvature, the inequality (53) will be satisfied which preserves the flow surface without any changes. As it can be observed in Fig. 6, the final stationary profiles of the granular mass are beneath its initial stationary profile.

4.2. The effects of the bed curvature and upwinding the source terms

Vázquez-Cendón [79] confirms the importance of upwinding the source terms containing the bed friction, T, and the bed level change, S_1. In this section, some of the experiments of Hutter et al. [47,48] are simulated with the present model to verify the importance of upwinding the source term S_2 including the effects of the bed curvature. These experiments included the release of a granular mass down a 40–60° straight slope, passing through a curved transition (246 mm radius) and depositing on a horizontal surface. Hutter et al. [47] considered two types of granular material: plastic particles with bulk density of 450 kg/m^3 representing snow avalanches and glass beads with density of 1730 kg/m^3 representing sand. The present model successfully estimated the flow thicknesses and velocities for both type of material. The computational errors of less than 4% for both flow height distribution (Eq. (57)) and flow velocities confirm the ability of the present model in estimating the properties of different types of granular flows.

The numerical results are compared with corresponding experimental data in Figs. 7 and 8 for experiment no. 113. In this experiment, the plastic particles are released on the 60° slope. The internal and basal friction angles are 29° and 23°, respectively and the model parameters are $\Delta x = 1.0$ and $r = 0.01$.

Fig. 7 shows the predicted depth flow profiles at different times from the beginning to deposition of the granular flow. The results demonstrate good agreement between the numerical and the experimental data with the computational error less than 5% for flow thickness distribution (Fig. 7a). As it mentioned in Section 2, the equations are transferred to a local coordinate system along the bed to consider the bed curvature effects on the sliding mass deformations. To illustrate the importance of the centripetal acceleration of the grains movement due to the bed curvature, the numerical results of the present model are compared with and without considering the bed curvature effects in Fig. 7a and b. The results indicate the strong effects of the interactions between the flow and the curved part on the granular flow properties. For a better visual comparison, the flow profiles and their corresponding velocities passing through the curved transition are illustrated in Fig. 7c and d, respectively. The curved part of the flume is located in the spacial interval of $x \in [80105]$. As it can be observed in Fig. 7c and d, the centrifugal forces acting on the flow through this part act like a local obstacle, slowing the flow, rising up the flow thickness and decreasing its energy. Both profiles (with and without considering the bed curvature) have the same velocity of about 42.8 m/s close to the curved part (Fig. 7d). With neglecting the bed curvature effects, avalanche passes through the curved part with an increased velocity of about 45 m/s to the horizontal part which leads to an up to 35% overestimated velocity on the horizontal part. Consequently, the granular mass deposits farther than the correct position on the flat surface (Fig. 7b). On the other hand, with considering the bed curvature effects, the granular mass flow is decelerated until it reaches to the velocity of about 29.8 m/s at the end of the curved part (Fig. 7d). The effects of this deceleration can be observed in Fig. 7c as increasing in the flow thickness compared with the flow thickness without curvature effects. This fact verifies that the curved part is acting like a local obstruction.

To compare the effects of centered discretization of the source terms with upwind discretization, the landslide deposit predicted based on upwinded source terms S_1 and S_2, centered source terms S_1 and S_2 and upwinded S_1 and centered S_2 are illustrated in Fig. 8. As it can be observed in this figure, with centered discretization of each source term, S_1 or S_2, or both the length of the avalanche deposition will be overestimated while its depth is simultaneously

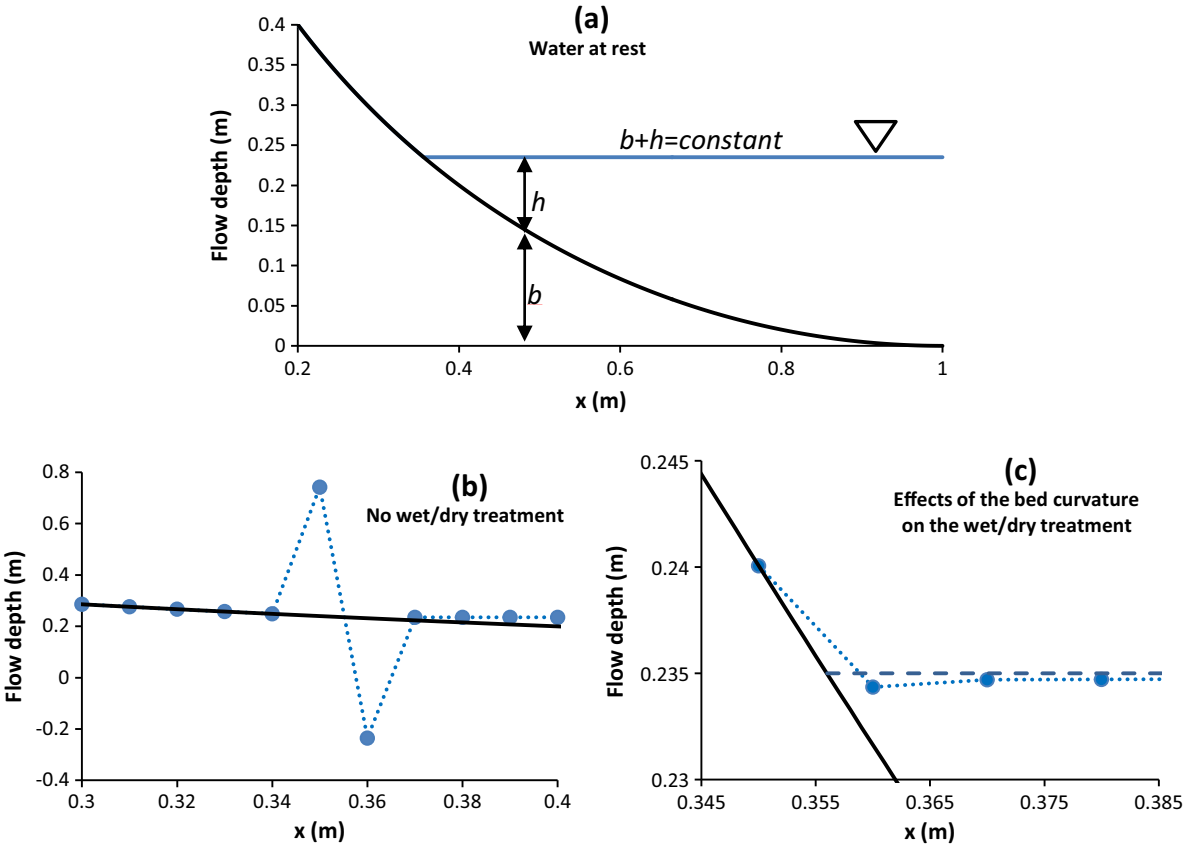

Fig. 5. The numerical results corresponding to water at rest. (a) Definition of the bed topography and the initial conditions. (b) Instability at the wet/dry front with considering no numerical treatment of wet/dry transition. (c) Numerical spurious movement at the flow surface caused by the source term related to the bed curvature.

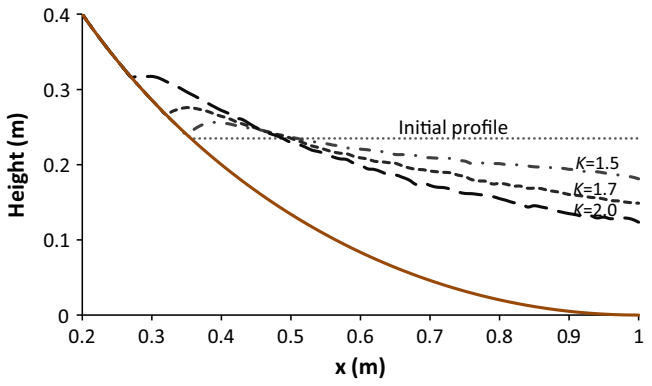

Fig. 6. Granular mass stationary profile with the constant basal friction angle of $\delta = 30^\circ$ against different values of the earth pressure coefficient, K.

underestimated (Table 2). These results can be a sign of artificial numerical dispersion which can be avoided by upwinding the source terms. Accordingly, like the other kinds of source terms, upwinding the source term S_2 related to the bed curvature decreases the artificial numerical dispersion and makes the stable region of the scheme bigger.

The numerical results of Hungr [43], who applied an integrated model based on a lagrangian numerical solution with the SH assumptions for the same problem, is also compared with the present model in Fig. 8. As it can be observed in this figure and Table 2, the present model estimates the maximum height, length and depth profile of the final deposition closer to the experimental data than the numerical results of Hungr [43]. The computational error of deposition profile in the last column of Table 2 is computed as

$$Err = \left(\sum_{i=1}^{m} |(h_{\exp_i} - h_{num_i})/h_{\exp_i}| \right) / (m+1) \quad (57)$$

where $h_{\exp_i}$ are the measured values and h_{num_i} are the computed values of deposition depths, and m is the number of computational grids.

As it can be observed in Fig. 7a, the solutions are free of numerical oscillations before the sliding mass starts to shape the final deposition. On the other hand, when the granular flow is slowing down to stop, the numerical results reveal some fluctuations on the avalanche surface (Figs. 6 and 8). These oscillations may be caused by the effects of critical stress which is trying to stop the granular flow when its angle is less than the angle of repose. Accordingly, the granular profile starts to change to a stable geometry which takes more time than the final deposition.

Finally, temporal positions of the flow leading edge are compared with the experimental measurements in Fig. 9. The computed values of the flow front position are in a good agreement with the experimental data with computational error less than 4%. As it mentioned before, when the effects of the bed curvature are neglected the flow velocity is overestimated by more than 35%.

It should be noticed that in all simulated experiments of Hutter et al. [47], the avalanche tail moves very slowly in comparison with the experimental measurements. It is probably due to considering a constant friction angle at the bottom, δ, while it dynamically reduces as the avalanche accelerates [1,38]. At high flow rates, the granular temperature may increase near the bottom boundary which leads to granular mass fluidization and consequent reduction of δ. On the other word, the front of a fully developed avalanche may acts like a granular solid, while its tail acts more like a fluid [50]. Moreover, Hungr [43] explained another

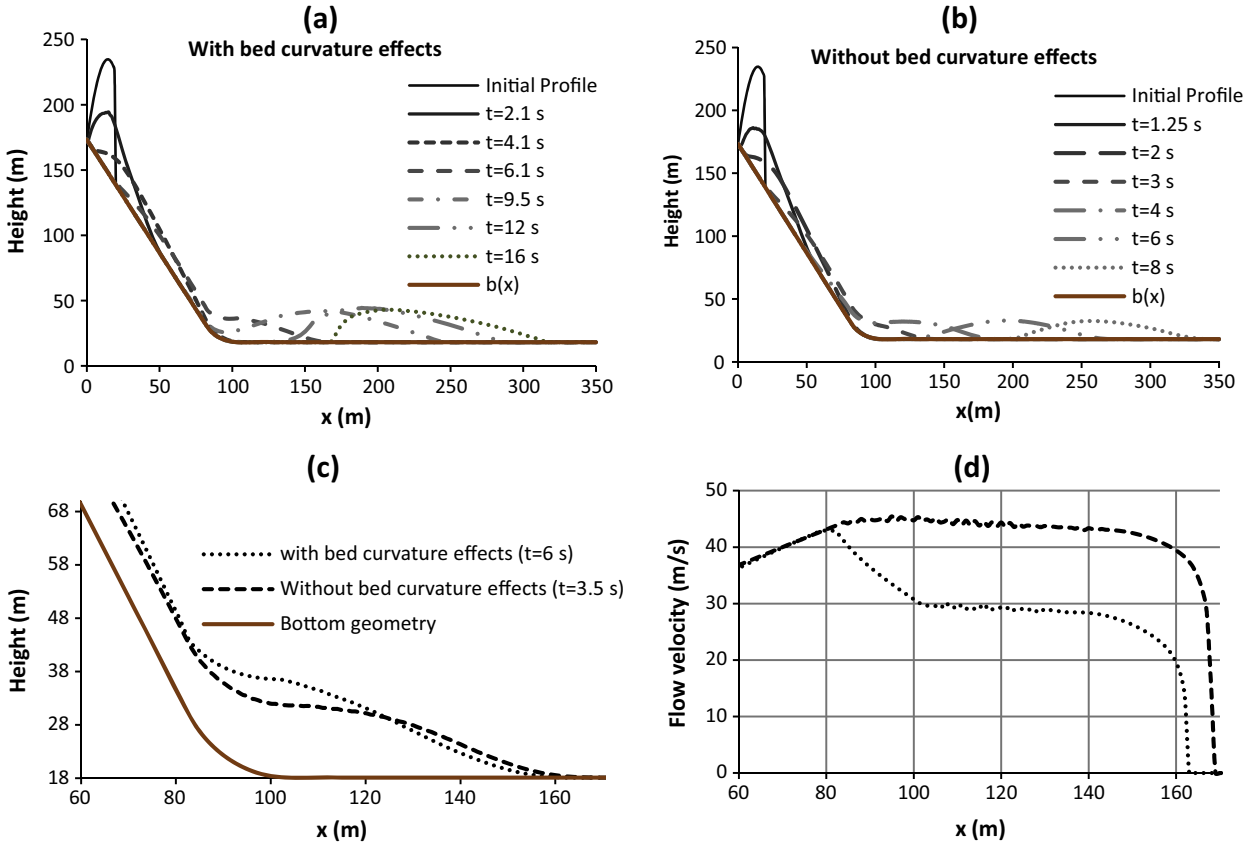

Fig. 7. Predicted flow profiles (a) including the bed curvature effects (0.1 s intervals) and (b) without the bed curvature effects (0.05 s intervals), for the experimental data of Hutter et al. [47] with the present model; (c) predicted depth flow profiles and (d) their corresponding flow velocities through the curved part of the flume. The flow depth is exaggerated 5 times.

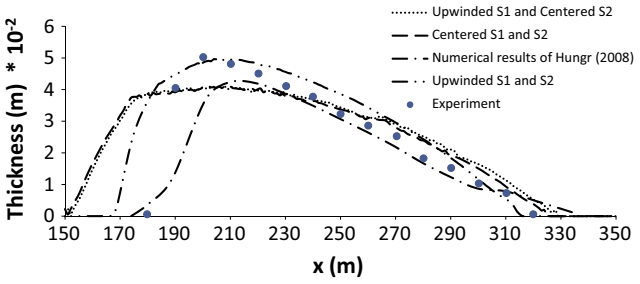

Fig. 8. Comparison between the predicted avalanche depositions with different discretization (upwind or centered) of the source terms and the numerical results of Hungr [33] for the experimental data of Hutter et al. [47].

Table 2
Relative errors (%) for computed values of deposit profile, length and maximum height; comparison between the numerical results of the present model with different discretization of the source terms, S_1 and S_2 and the numerical results of Hungr [43] with the experiment no. 113 of Hutter et al. [47].

Numerical considerations	Maximum height	Deposition length	Depth profile
Upwinded S_1 and S_2	1.80	7.72	4.15
Centered S_1 and S_2	18.41	24.85	9.08
Upwinded S_1 and centered S_2	18.34	26.28	9.29
Hungr [33]	15.59	15.83	7.96

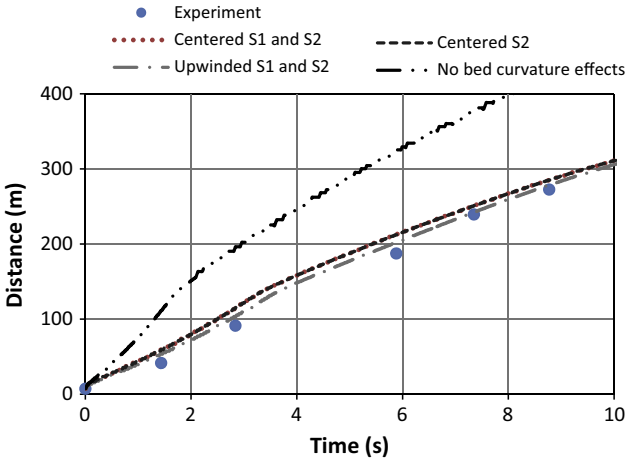

Fig. 9. Comparison between the present numerical results and the experimental data of Hutter et al. [47] for flow front position against time. The numerical results are based on considering: upwinded S_1 and centered S_2, centered S_1 and S_2, upwinded S_1 and S_2 and no bed curvature effects.

shortcoming of SH model, i.e. considering negligible depth gradients due to shallow flow assumption of parallel flow lines, which is a further effective factor in slowing down the trailing flow [43]. The curved flow lines caused by a significant depth gradient create a pressure component nonparallel to the bed. This pressure component originates additional shear stresses close to the bottom which are not considered in classic SH model. He proposed a modified definition for the resisting shear stress at the flow bottom with reducing the basal friction angle by a certain fraction of this additional stress [43]. Underestimated velocities of ensuing flow affect the maximum travel distance (1.25% underestimated) and

especially the final deposition length (7.72% overestimated) of the slide. Proper estimation of trailing flow behavior is important to predict the topographic changes of the bottom after landslide. Nevertheless, the primary purpose of natural granular flow modeling is to estimate their maximum possible travel distance and the prediction of flow tail is of less practical importance. This fact makes the present model an applicable means for analyzing the real hazards.

4.3. Adverse slope

Predicting the behavior of granular flow against protective structures such as barriers is an important aspect of risk assessment [57,62,66]. It is also applicable for testing the wet/dry treatment method when the flow is going up against a slope. The ability of the proposed numerical framework in estimating the maximum runup against an obstacle is verified by simulating one of the experiments performed by Mancarella and Hungr [57]. In these experiments, a reservoir of dry sand with the bulk density of 1630 kg/m^3 is released down a 29° slope, passing through a curved transition with the radius of 0.1 m and running into an adverse 33° slope [57]. The internal and basal friction angles are measured as 30.9° and 21.7°, respectively [57].

The final profile of the granular flow and the flow front velocities are shown in Fig. 10, with and without considering numerical treatment for wet/dry transitions. The numerical results are in a good agreement with corresponding experimental data with computational error less than 4% for the flow thicknesses. As it can be observed in Fig. 10b, the granular flow reaches to the maximum distance of 1.86 m on the reversed slope at time 1.35 s which is sufficiently close to the experimental measurements of about 1.83 m at time 1.2 s with relative error of about 1.64%. Without considering any wet/dry treatment, the maximum runup and the flow velocity are overestimated by more than 5% and 20%, respectively.

4.4. Critical flow

A simple dam break problem is simulated with the present model to show the effects of applying the critical flow fix (CFF) method. A 0.2 m high, 0.4 m long reservoir of sand is suddenly released down a dry bed [43]. The granular material has the bulk density of 1630 kg/m^3 with the inertial friction angle of $\phi = 31.9°$ and the basal friction angle of $\delta = 21.7°$ [43].

Comparison between the numerical and the experimental data can be observed in Fig. 11. The granular flow is critical around the gate, $x = 0.4$ m in Fig. 11a, where the Froude number is one (Fig. 11b). In this area without using the CFF method, the scheme is not able to show the flow profile correctly due to vanishing one of the eigenvalues of the Jacobean matrix A. With increasing the near zero eigenvalue by applying the CFF correction, the numerical results become correct and smooth enough. Fig. 11c and d shows the final profile of granular material and its equivalent Froude numbers, respectively. When the flow becomes subcritical, $Fr < 1$, all over the computational domain (Fig. 11d), the scheme works properly even without CFF correction. Anyway, the effects of incorrect fluxes at critical regions make the numerical results far away from the experimental results (Fig. 11c).

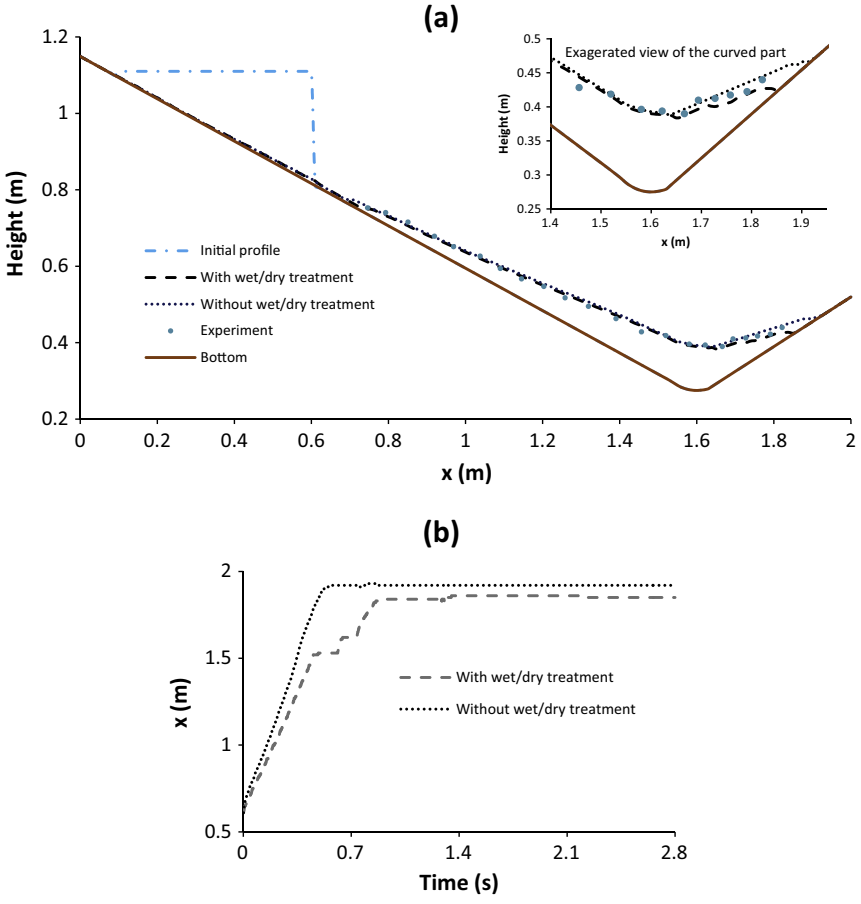

Fig. 10. Comparison between the numerical and experimental (a) flow deposit distribution and (b) flow front positions against time for the experiments of Mancarella and Hungr [57]. The numerical results are shown with and without considering the wet/dry numerical treatment.

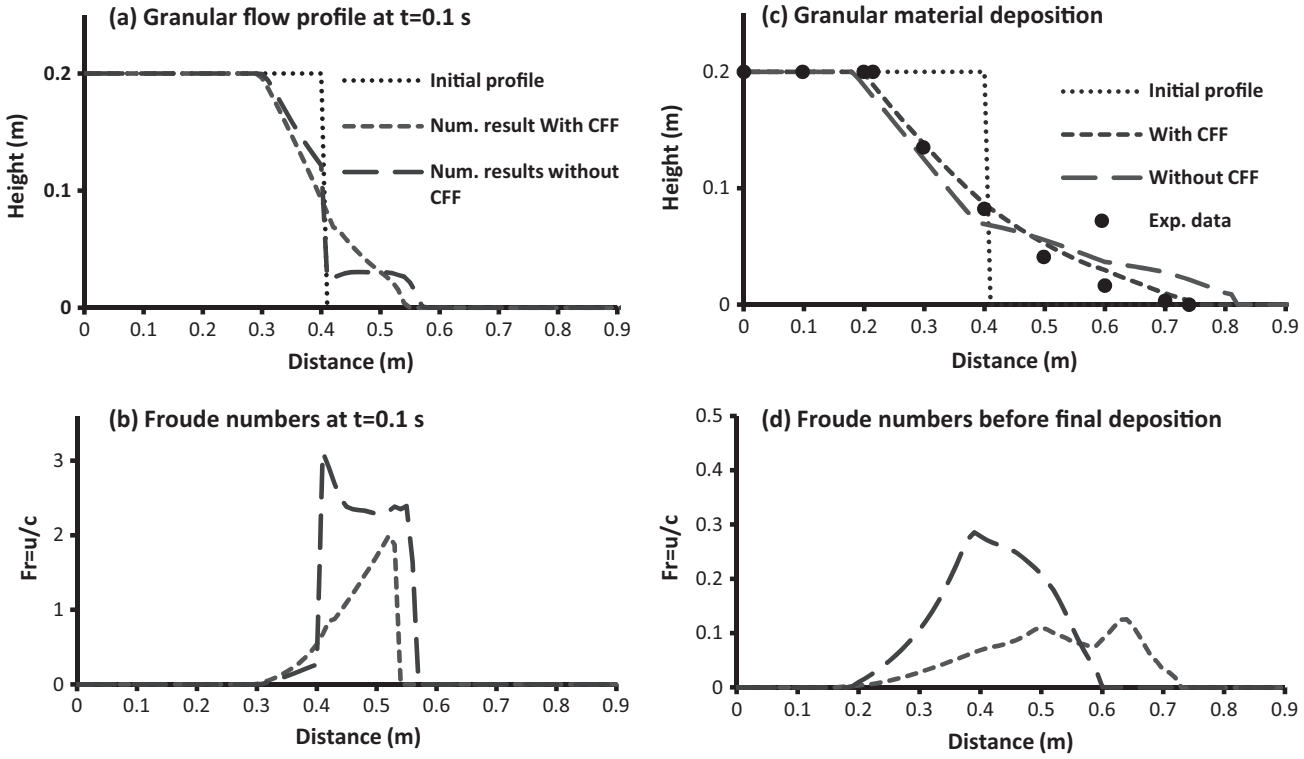

Fig. 11. Comparison between the numerical results of the proposed scheme (a) and (b) with and (c) and (d) without critical flow fix (CFF) and the experimental data of Hungr [43].

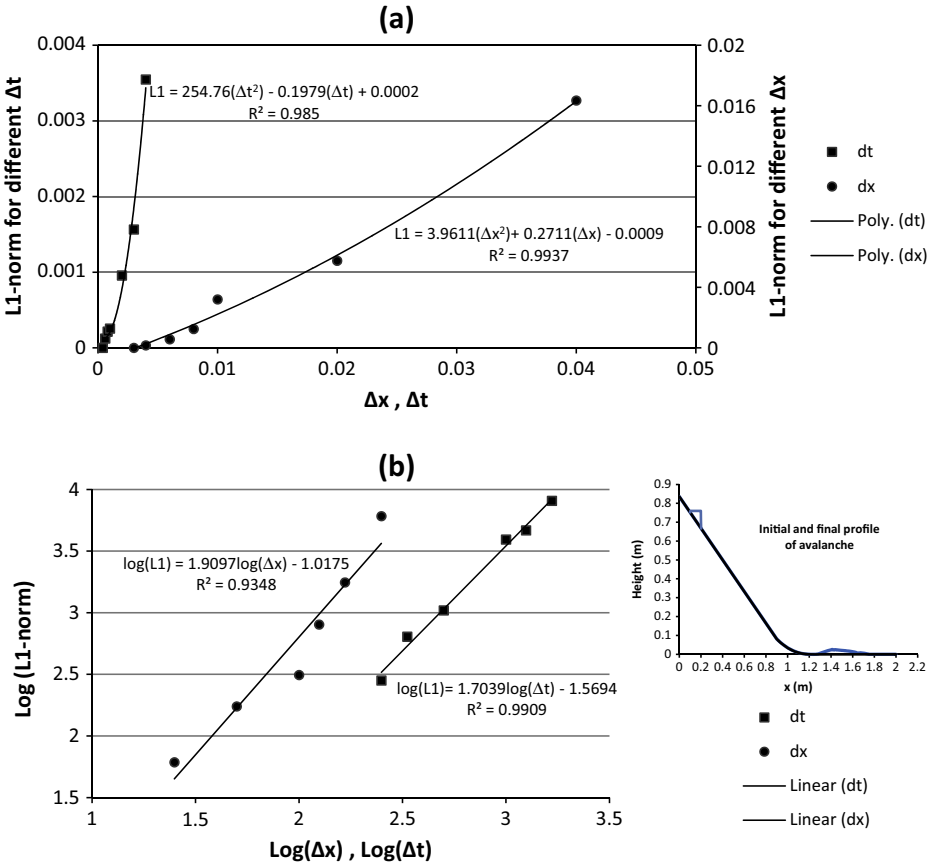

Fig. 12. (a) The absolute error values (L_1-norm) and (b) the log–log graph of L_1-norm plotted against different values of Δx and Δt.

4.5. Order of accuracy

The following numerical test is performed by the present model to illustrate the decreasing trend of the scheme error against different time steps, Δt, and mesh sizes, Δx. As it can be observed in the right side of Fig. 12b, a wedge-shaped granular mass with the same length and height of 0.1 m is released down a 40° slope passing through a curved transition (0.6 m radius) to a horizontal plane. The inclined, curved and straight parts of the considered topography are 1.175 m, 0.314 m and 0.8 m long, respectively. The internal and the basal friction angles are supposed to be 30° and 23°, chosen as common values of friction angles for dry sand, respectively [47,74]. The values of flow thickness corresponding to the final granular mass profile (avalanche deposit) are applied to calculate the numerical errors. The sum of absolute difference (L_1-norm) [55] of the flow thicknesses is calculated for different values of time steps, Δt, or mesh sizes, Δx, as [55]

$$L_1 = \|h_1 - h_2\|_1 = \sum_{i=1}^{m} |h_{1,i} - h_{2,i}| \tag{58}$$

where h_1 is the predicted flow thickness and m is the number of computational mesh points. h_2 is equal to the exact values of flow depth which in case are supposed to be the predicted values for $\Delta x = 0.003$ and $\Delta t = 0.001$ to compare the L_1-norm based on different values of Δx and for $\Delta x = 0.01$ and $\Delta t = 0.0004$ to compare the L_1-norm based on different values of Δt.

The computed errors against both time step and cell size are plotted in Fig. 12. As it can be observed in Fig. 12a, the absolute error (L_1-norm) of the present scheme has an approximate second order descending trend against decreasing both Δx and Δt. In Fig. 12b, the absolute errors are plotted against different length steps and time steps in a log–log graph. According to this figure, the slopes of the error curves are about 1.91 against Δx and 1.7 against Δt. The difference of these slopes with the expected value of 2 represents the existence of other sources of error. With considering a constant Δx or Δt and changing the other one, we have different values of $r = \Delta t/\Delta x$ which has noticeable effects on numerical results regarding avalanche properties and its deposit profile. Therefore, it may change the consequent computational errors. Besides, in the present model the granular mass has stop points where its angle is less than the angle of repose. This stop points also change the granular mass properties. They may happen everywhere along the flow path depending on various factors such as avalanche depth and velocity, internal and basal friction angle, model parameters (Δx, Δt and r) and bottom topography. Finally, it should be remembered that error curves are plotted in log scale so a modest difference on the error values can correspond to a very large difference in magnitude.

5. Conclusions

In this work, we introduced a numerical solution of granular type flows based on shallow SH type model using a well-balanced Roe type finite volume scheme. The model is derived in a local coordinate system along the non-erodible bottom to consider its curvature effects. The proposed scheme is based on the Q-scheme of Roe, and upwinding the source terms related to the bottom level and the bed curvature. Numerical results confirm the strong effects of the bed curvature on the granular flow characteristics and the importance of upwinding the source term corresponding to the bed curvature like the other source term. Centered discretization of this source term can originate numerical spurious waves and artificial dispersion. The numerical method constructed in this way completely satisfies the C-property.

The Coulomb friction term is discretized using a two-step semi-implicit approach. This approach prepares the proposed scheme to simulate the static regions caused by frictional resistance of the non-erodible bed maintaining stability. These static areas may appear when the flow is supposed to be shallow. In the present model, the basal friction angle is supposed to be constant which is unrealistic. To have a better estimate of flow velocities especially at the flow trail, a time-dependent relation can be considered for the basal friction angle based on grain temperature and grain-size segregation.

Different situations of wet/dry transitions are numerically treated in the present model. In this model both the bed level and the bed curvature are considered into the equations. Accordingly, it is proposed to neglect the bed curvature at the left and the right sides of the related intercell to calculate the numerical fluxes. This idea is verified by the numerical results. This modified wet/dry algorithm helps the proposed scheme to avoid appearance of negative flow thickness and overestimated flow velocities. Moreover, the scheme is able to satisfy stationary solutions including wet/dry fronts.

Our numerical results demonstrate the efficiency of the proposed numerical framework in reducing non-physical results like negative flow heights, spurious numerical waves and artificial numerical dispersion which are the main concerns in numerical modeling of fluid flows. Comparison with the available experimental measurements shows that the present model applying this modified scheme estimates the granular flow thickness, velocity and maximum run-up with a relative error of less than 5%. These results confirm the ability of the proposed method for natural landslide hazards analysis. Although we have limited our investigation to the case of one dimensional mathematical model in this study, our methodology is applicable to multi-dimensional models. In particular, the procedure can be extended for multi-layer cases as well.

Acknowledgements

The first author is grateful for the support of Civil and Environmental engineering department of University of California, Irvine, during her research visit. The authors wish to thank the Editor-in-Chief Professor Griffiths for his thoughtful comments and also two anonymous reviewers for their constructive comments which helped to improve the final manuscript.

References

[1] Ancey Ch. Plasticity and geophysical flows: a review. J Non-Newtonian Fluid Mech 2007;142:4–35. http://dx.doi.org/10.1016/j.jnnfm.2006.05.005.
[2] Aranson IS, Tsimring S. Continuum theory of partially fluidized granular flows. Phys Rev E 2002;65. http://dx.doi.org/10.1103/physRevE.65.061303. 061303(1-20).
[3] Armanini A, Fraccarollo L, Rosatti G. Two-dimensional simulation of debris flows in erodible channels. Comput Geosci 2009;35:993–1006. http://dx.doi.org/10.1016/j.cageo.2007.11.008.
[4] Armanini A, Larcher M, Nucci E, Dumbser M. Submerged granular channel flows driven by gravity. Adv Water Resour 2014;63:1–10. http://dx.doi.org/10.1016/j.advwatres.2013.10.007.
[5] Ataie-Ashtiani B, Jalali-Farahani R. Improvement and application of I-SPH method in the simulation of impulsive waves. In: Proceedings of the international conference on violent flows, Fukuoka, Japan; 2007. p. 116–21.
[6] Ataie-Ashtiani B, Malek-Mohammadi S. Near field amplitude of sub-aerial landslide generated waves in dam reservoirs. Dam Eng 2007;XVII(4):197–222.
[7] Ataie-Ashtiani B, Malek-Mohammadi S. Mapping impulsive waves due to subaerial landslides into a dam reservoir: case study of Shafa-Roud dam. Dam Eng 2008;XVIII(3):1–25.
[8] Ataie-Ashtiani B, Mansour-Rezaei S. Modification of weakly Compressible Smoothed Particle Hydrodynamics for preservation of angular momentum in simulation of impulsive wave problems. Coastal Eng J 2009;51(4):363–86.
[9] Ataie-Ashtiani B, Najafi-Jilani A. Prediction of submerged landslide generated waves in dam reservoirs: an applied approach. Dam Eng 2006;XVII(3):135–55.
[10] Ataie-Ashtiani B, Najafi-Jilani A. A higher-order Boussinesq-type model with moving bottom boundary: applications to submarine landslide tsunami waves. Int J Numer Methods Fluids 2007;53(6):1019–48.

[11] Ataie-Ashtiani B, Nik-khah A. Impulsive waves caused by subaerial landslides. Environ Fluid Mech 2008;8(3):263–80.
[12] Ataie-Ashtiani B, Shobeiry G. Numerical simulation of landslide impulsive waves by modified smooth particle hydrodynamics. Int J Numer Methods Fluids 2008;56(2):209–32.
[13] Ataie-Ashtiani B, Shobeiry G, Farhadi L. Modified incompressible SPH method for simulating free surface problems. Fluid Dyn Res 2008;40(9):637–61.
[14] Ataie-Ashtiani B, Yavari-Ramshe S. Numerical simulation of wave generated by landslide incidents in dam reservoirs. Landslides 2011;8:417–32. http://dx.doi.org/10.1007/s10346-011-0258-8.
[15] Begnudelli L, Sanders BF. Unstructured grid finite-volume algorithm for shallow-water flow and scalar transport with wetting and drying. J Hydraul Eng ASCE 2006;132(4):371–84. http://dx.doi.org/10.1061/(ASCE)0733-942(2006) 132:4(371).
[16] Bermudez A, Vazquez-Cendon ME. Upwind methods for hyperbolic conservation laws with source terms. Comput Fluids 1994;23(8):1049–71.
[17] Berthon C, Marche F, Turpault R. An efficient scheme on wet/dry transitions for shallow water equations with friction. Comput Fluids 2011;48(1):192–201. http://dx.doi.org/10.1016/j.compfluid.2011.04.011.
[18] Bertolo P, Bottino G. Debris-flow event in the Frangerello Stream-Susa valley (Italy) – calibration of numerical models for the back analysis of the 16 October, 2000 rainstorm. Landslides 2008;5:19–30. http://dx.doi.org/10.1007/s10346-007-0099-7.
[19] Botz JT, Loudon C, Barger JB, Olafsen JS, Steeples DW. Effects of slope and particle size on ant locomotion: implications for choice of substrate by antlions. J Kans Entomol Soc 2003;76(3):426–35.
[20] Bouchut F, Mangeney-Castelnau A, Perthame B, Vilotte JP. A new model of Saint Venant and Savage–Hutter type for gravity driven shallow flows. C R Acad Sci Paris, Ser I 2003;336:531–6.
[21] Bradford SF, Sanders BF. Finite-volume model for shallow-water flooding of arbitrary topography. J Hydraul Eng 2002;2002(128):289–98. http://dx.doi.org/10.1016/(ASCE)0733-9429128:3(289).
[22] Brufau P, Vázquez-Cendón ME, García-Navarro P. A numerical model for the flooding and drying of irregular domain. Int J Numer Methods Fluids 2002;39:247–75.
[23] Brufau P, García-Navarro P, Ghilardi P, Natale L, Savi F. 1D mathematical modeling of debris flow. J Hydraul Res 2000;38(6):435–46.
[24] Castro MJ, Ferreiro AM, García-Rodríguez JA, González-Vida JM, Macías J, Parés C, et al. The numerical treatment of wet/dry fronts in shallow flows: application to one-layer and two-layer systems. Math Comput Model 2005;42:419–32. http://dx.doi.org/10.1016/j.mcm.2004.01.016.
[25] Castro MJ, González-Vida JM, Parés C. Numerical treatment of wet/dry fronts in shallow flows with a modified roe scheme. Math Models Methods Appl Sci 2005;16:897. http://dx.doi.org/10.1142/S021820250600139X.
[26] Castro M, Macías J, Parés C. A Q-scheme for a class of systems of coupled conservation laws with source term. Application to a two-layer 1-D shallow water system. J Math Model Numer Anal 2003;35:107–27.
[27] Chauchat J, Medale M. A three-dimensional numerical model for dense granular flows based on the μ(1) rheology. J Comput Phys 2014;256:696–712. http://dx.doi.org/10.1016/j.jcp.2013.09.004.
[28] Chen H, Lee CF. A dynamic model for rainfall-induced landslides on natural slopes. Geomorphology 2003;51:269–88. http://dx.doi.org/10.1016/S0169-555X(02)00224-6.
[29] Courant R, Friedrichs K, Lewy H. On the partial difference equations of mathematical physics. IBM J Res Dev 1928;11(2):215–34.
[30] Denlinger RP, Iverson RM. Flow of variably fluidized granular masses across 3-D terrain: 2. Numerical predictions and experimental tests. J Geophys Res 2001;106(B1):553–66.
[31] Denlinger RP, Iverson RM. Granular avalanches across irregular three-dimensional terrain: 1. Theory and computation. J Geophys Res 2004;109:F01014. http://dx.doi.org/10.1029/2003JF00008.
[32] Domnik B, Pudasaini SP, Katzenbach R, Miller SA. Coupling of full two-dimensional and depth-averaged models for granular flows. J Non-Newtonian Fluid Mech 2013;201:56–68. http://dx.doi.org/10.1016/j.jnnfm.2013.07.005.
[33] Duman TY. The largest landslide dam in Turkey: Tortum landslide. Eng Geol 2009;104:66–79. http://dx.doi.org/10.1016/j.enggeo.2008.08.006.
[34] Fernández-Nieto ED, Bouchut F, Bresch B, Castro Díaz MJ, Mangeney A. A new Savage–Hutter type model for submarine avalanches and generated tsunami. J Comput Phys 2008;227:7720–54.
[35] Frenette R, Zimmermann T, Eyheramendy D. Unified modeling of fluid or granular flows on dam-break case. J Hydraul Eng 2002;128:299–305. http://dx.doi.org/10.1061/(ASCE)0733-9429(2002) 128:3(299).
[36] Fritz HM, Mohammed F, Yoo J. Lituya bay landslide impact generated mega-tsunami 50th anniversary. Pure Appl Geophys 2009;166:153–75.
[37] Glaister P. Approximate Riemann solutions of the shallow water equations. J Hydraul Res 1988;26(3):293–306. http://dx.doi.org/10.1080/00221688809499213.
[38] Gray JMNT, Wieland M, Hutter K. Gravity-driven free surface flow of granular avalanches over complex basal topography. Proc R Soc Lond A 1999;455:1841–74.
[39] Greve R, Hutter K. Motion of a granular avalanche in a convex and concave curved chute: experiments and theoretical predictions. Philos Trans R Soc Lond 1993;342:573–600.
[40] Harten A, Lax P, Van Leer B. On upstream differencing and Godunov-type schemes for hyperbolic conservation laws. SIAM Rev 1983;25:35–61. http://dx.doi.org/10.1137/1025002.
[41] Harten A. On a class of high resolution total-variation-stable finite-difference schemes. SIAM J Numer Anal 1984;21:1–23.
[42] Hungr O. A model for the runout analysis of rapid flow slides, debris flows, and avalanches. Can Geotech J 1995;32:610–23.
[43] Hungr O. Simplified models of spreading flow of dry granular material. Can Geotech J 2008;45:1156–68. http://dx.doi.org/10.1139/T08-059.
[44] Hungr O, Morgenstern NR. Experiments on the flow behavior of granular materials at high velocity in an open channel. Geotechnique 1984;34:405–13.
[45] Hutter K, Greve R. Two-dimensional similarity solutions for finite-mass granular avalanches with Coulomb- and viscous-type frictional resistance. J Glaciol 1993;39:357–72.
[46] Hutter K, Koch T. Motion of a granular avalanche in an exponentially curved chute: experiments and theoretical predictions. Philos Trans R Soc Lond 1991;334:93–138.
[47] Hutter K, Koch T, Plüss C, Savage SB. The dynamics of avalanches of granular materials from initiation to runout. Part II. Experiments. Acta Mech 1995;109:127–65.
[48] Hutter K, Savage S, Nohguchi Y. Numerical, analytical, and laboratory experimental studies of granular avalanche flows. Ann Glaciol 1989;13:109–16.
[49] Imran J, Harff P, Parker G. A numerical model of submarine debris flow with graphical user interface. Comput Geosci 2001;27:717–29.
[50] Iverson RM. The physics of debris flows. Rev Geophys 1997;35(3):245–96.
[51] Iverson RM, Vallance JW. New views of granular mass flows. Geology 2001;29(2):115–8.
[52] Koch T, Greve R, Hutter K. Unconfined flow of granular avalanches along a partly curved surface, Part II: Experiments and numerical computations. Proc R Soc Lond A 1994;445:415–35.
[53] Laigle D, Coussot Ph. Numerical modeling of mudflows. J Hydraul Eng 1997;123:617–23.
[54] Lax PD, Wendroff B. Systems of conservation laws. Commun Pure Appl Math 1960;13(2):217–37. http://dx.doi.org/10.1002/cpa.3160130205.
[55] LeVeque RJ. Finite volume methods for hyperbolic problems. Cambridge (UK): Cambridge University Press; 2002.
[56] Liang Q, Borthwick AGL. Adaptive quadtree simulation of shallow flows with wet–dry fronts over complex topography. Comput Fluids 2009;38:221–34. http://dx.doi.org/10.1016/j.compfluid.2008.02.008.
[57] Mancarella D, Hungr O. Analysis of run-up of granular avalanches against steep, adverse slopes and protective barriers. Can Geotech J 2010;47:827–41. http://dx.doi.org/10.1139/T09-143.
[58] Mangeney-Castelnau A, Vilotte JP, Bristeau MO, Perthame B, Bouchet F, Siomeoni C, et al. Numerical modeling of avalanches based on Saint Venant equations using a kinetic scheme. J Geophys Res 2003;108(B11):2527. http://dx.doi.org/10.1029/2002JB002024.
[59] McDougall S, Hungr O. A model for the analysis of rapid landslide motion across three-dimensional terrain. Can Geotech J 2004;41:1084–97. http://dx.doi.org/10.1139/T04-052.
[60] Medeiros S, Hagon SC. Review of wetting and drying algorithms for numerical tidal flow models. Int J Numer Methods Fluids 2013;71:473–87. http://dx.doi.org/10.1002/fld.3668.
[61] Medina VM, Bateman A, Hürlimann M. A 2D finite volume model for debris flow and its application to events occurred in the Eastern Pyrenees. Int J Sediment Res 2008;23(4):348–60.
[62] Moriguchi Sh, Borja RI, Yashima A, Sawada K. Estimating the impact force generated by granular flow on a rigid obstruction. Acta Geotech 2009;4:57–71. http://dx.doi.org/10.1007/s11440-009-0084-5.
[63] Panizzo A, De Girolamo P, Di Risio M, Maistri A, Petaccia A. Great landslide events in Italian artificial reservoirs. Nat Hazards Earth Syst Sci 2005;5:733–40.
[64] Pankow KL, Moore JR, Hale JM, Koper D, Kubacki T, Whidden KM, et al. Massive landslide at Utah copper mine generates wealth of geophysical data. GSA Today 2014;24(1):4–9. http://dx.doi.org/10.1130/GSATG191A.1.
[65] Pitman EB, Nichita CC, Patra A, Bauer A. Computing granular avalanches and landslides. Phys Fluids 2003;15(12):3638–46. http://dx.doi.org/10.1063/1.1614253.
[66] Pudasaini ShP, Kröner C. Shock waves in rapid flows of dense granular materials: theoretical predictions and experimental results. Phys Rev 2008;E78:041308. http://dx.doi.org/10.1103/PhysRevE.78.041308.
[67] Pudasaini ShP, Wang Y, Sheng LT, Hsiau SS, Hutter K, Katzenbach R. Avalanching granular flows down curved and twisted channels: theoretical and experimental results. Phys Fluids 2008;20:073302. http://dx.doi.org/10.1063/1.2945304.
[68] Roe PL. Approximate Riemann solver, parameter vectors, and difference schemes. J Comput Phys 1981;43:357–72. http://dx.doi.org/10.1016/0021-9991(81)90128-5.
[69] Roe PL. Upwind differenced schemes for hyperbolic conservation laws with source terms. In: Carasso, Raviart, Serre, editors. Proceedings of the conference on hyperbolic problems. Springer; 1986. p. 41–51.
[70] Savage SB, Hutter K. The motion of a finite mass of granular material down a rough incline. J Fluid Mech 1989;199:177–215.
[71] Savage SB, Hutter K. The dynamics of avalanches of granular materials from initiation to runout. Part I: Analysis. Acta Mech 1991;86:201–23.
[72] Takagi D, McElwaine JM, Huppert HE. Shallow granular flows. Phys Rev E 2011;83:031306-1–031306-10. http://dx.doi.org/10.1103/PhysRevE.83.031306.

[73] Tannehill JC, Anderson DA, Pletcher RH. Computational fluid mechanics and heat transfer. Series in computational and physical processes in mechanics and thermal sciences. Taylor & Francis Publishers; 1997.
[74] Terzaghi K, Peck RB, Mesri G. Soil mechanics in engineering practice. John Wiley & Sons; 1996.
[75] Toni SD, Scotton P. Two-dimensional mathematical and numerical model for the dynamics of granular avalanches. Cold Reg Sci Technol 2005;43:36–48. http://dx.doi.org/10.1016/j.coldregions.2005.05.002.
[76] Toro EF. Riemann solvers and numerical methods for fluid dynamics. 2nd ed. Springer-Verlag; 1999.
[77] Toro EF. Shock-capturing methods for free-surface shallow flows. John Wiley & Sons; 2001.
[78] Van Leer B, Lee WT, Powell KG. Sonic point capturing. In: 9th Computational fluid dynamics conference. American Institute of Aeronautics and Astronautics, Buffalo, NY; 1989.
[79] Vázquez-Cendón ME. Improved treatment of source terms in upwind schemes for the shallow water equations in channels with irregular geometry. J Comput Phys 1999;148:497–526.
[80] Watts Ph, Grilli ST, Tappin DR, Freyer GJ. Tsunami generation by submarine mass failure. II: Predictive equations and case studies. J Waterway, Port, Coastal, Ocean Eng 2005;131(6):298–310. http://dx.doi.org/10.1061/(ASCE)0733-950X(2005) 131:6(298).
[81] Wieland M, Gray MNT, Hutter K. Channelized free-surface flow of cohesionless granular avalanches in chute with shallow lateral curvature. J Fluid Mech 1999;392:73–100.
[82] Yavari-Ramshe S, Ataie-Ashtiani B. Simulation of wave generated by landslides in Maku dam reservoir. In: Oka F, Kimoto S, Murakami O, editors. Prediction and simulation methods for geohazard mitigation. CRC Press; 2009 [chapter 14].
[83] Zanuttigh B, Lamberti A. Analysis of debris wave development using 1D shallow water equations. J Hydraul Eng 2004;1304:293–304.